

THE ELECTRONIC STRUCTURE OF SEMICONDUCTOR NANOCRYSTALS¹

Al. L. Efros and M. Rosen

Nanostructure Optics Section, Naval Research Laboratory, Washington, DC; e-mail: efros@ccfsun.nrl.navy.mil; rosen@ccfsun.nrl.navy.mil

Key Words optical properties, quantum size levels, exchange interaction, magnetic dopant

■ **Abstract** We review the rapid progress made in our understanding of the crystal properties of semiconductors and nanocrystals focussing on theoretical results obtained within the multiband effective mass approximation. A comparison with experiment shows these results are valid for nanocrystals down 22–26 Å in diameter. The effect of the electron-hole Coulomb interaction on the optical spectra is analyzed. A theory of the quantum-size levels in wide gap (CdSe) and narrow gap semiconductors (InAs) is presented that describes the absorption spectra of these semiconductors well. A great enhancement of the electron-hole exchange interaction leads to the formation of the optically forbidden Dark Exciton in nanocrystals, which strongly affects their photoluminescence. A theory of the band-edge exciton fine structure is presented and applied to the study of the PL in CdSe nanocrystals. The effect of doping on nanocrystal spectra is considered. The enhancement of the short-range spin-spin interaction in Mn-doped nanocrystals leads to a giant splitting of the electron and hole spin sublevels.

INTRODUCTION

This review summarizes the rapid progress in the physical understanding of the linear optical properties of semiconductor nanocrystals made in the last 10 to 15 years. A wide class of semiconductor materials has been prepared in nanocrystal form, including covalent Si and Ge, III-V semiconductor compounds (GaAs, GaP, InP), II-VI compounds (CdSe, CdS, ZnSe, CdTe, PbS and their alloys), and I-VII compounds (CuCl, CuBr, AgBr). Furthermore, current technology allows control of the size, shape, and surface of these nano-size semiconductor crystals. We discuss the intrinsic electronic properties of nanocrystals that effect photo absorption and photoluminescence in these materials, as well as the

¹The US Government has the right to retain a nonexclusive, royalty-free license in and to any copyright covering this paper.

effect of doping of nanocrystals. All these properties depend strongly on the nanocrystal radius. This paper is focused on theoretical descriptions of electronic structure of semiconductor nanocrystals. One can find a broad description of the experimental investigations of nano-size semiconductor crystals and their potential applications in the excellent reviews of Brus (1) and Alivisatos (2).

The size dependence of semiconductor nanocrystal optical properties was discovered independently almost two decades ago in two different materials: in semiconductor-doped glasses by Ekimov et al (3), and in colloidal solutions by Henglein (4). In both cases it was shown that the color of the nanocrystals strongly correlates with their size. Also for both cases the growth of the nanocrystals is the result of the thermodynamic process of microscopic phase separation in a supersaturated solution. The size of the nanocrystals—the nuclei of the new phase—is controlled by diffusion of the atoms or ions to the growing nucleus and the degree of supersaturation. The final size distribution of the semiconductor nanocrystals is determined by the duration of the phase separation process and is fixed at its interruption. This process is termed arrested precipitation. A similar type of the nanocrystal growth was later shown (5) to be possible in semiconductor crystal lattices as well as in liquid and solid solutions.

The size dependence of the nanocrystal absorption and luminescence spectra is determined by the quantum-size effect, which drastically modifies the energy spectra of three-dimensionally confined quasiparticles. Both linear and nonlinear optical properties of small semiconductor nanocrystals arise as a result of transitions between electron and hole quantum-size levels (QSLs). In a spherical nanocrystal surrounded by an infinite potential barrier, the energy of the electron and hole quantum-size levels, characterized by angular momentum quantum number l , can be written in parabolic approximation as (6, 7)

$$E_{l,n}^{e,h} = \frac{\hbar^2 \phi_{l,n}^2}{2m_{e,h} a^2}, \quad 1.$$

where $m_{e,h}$ is the electron and hole effective mass respectively, a is the crystal radius, $\phi_{l,n}$ is the n th root of the spherical Bessel function of order l $j_l(\phi_{l,n}) = 0$ (the four lowest roots are $\phi_{0,0} = \pi$, $\phi_{1,0} \approx 4.49$, $\phi_{2,0} = 5.76$, and $\phi_{0,1} = 2\pi$, respectively). The energy of the lowest electron and hole quantum-size levels increases with decreasing nanocrystal size and, hence, increases the total energy of the band edge optical transitions. For example, in CdSe nanocrystals, this shift of the energy gap reaches 1.2 eV. By changing the nanocrystal size we can vary the energy gap of this material from 1.8 eV, its bulk value, up to 3 eV, passing through almost the whole visual part of the optical spectrum (7a).

However, the Coulomb interaction between the optically created electron and hole strongly affects the nanocrystal optical spectra. This interaction must always be taken into account because both particles are confined in the same crystal volume. The Coulomb energy of the electron and hole interaction is on the order of $e^2/\kappa a$, where κ is the dielectric constant of the semiconductor. Because

the quantization energy increases with decreasing size as $1/a^2$, the Coulomb energy, which grows only as $1/a$, becomes a small correction to the quantization energies of electrons and holes in small crystals and reduces transition energies by only a relatively small amount. On the other hand, in large nanocrystals, the Coulomb interaction is more important than the quantization energies of the electrons and holes. Theoretical analysis shows that the optical properties of nanocrystals strongly depend on the ratio of the nanocrystal radius, a , to the Bohr radius of the bulk exciton, $a_B = \hbar^2 \kappa / \mu e^2$, where μ is the exciton reduced mass (6, 8). In the analysis of experimental data, one needs to consider three different regimes: $a \gg a_B$, $a \sim a_B$, and $a \ll a_B$.

Weak Confinement Regime

In the case $a \gg a_B$, the binding energy of an exciton, E_{ex} , is larger than the quantization energy of both the electrons and holes, and the optical spectra of these nanocrystals are determined by the quantum confinement of the exciton center of mass. The exciton ground state energy is given by (6)

$$\hbar\omega = E_g - E_{ex} + \frac{\hbar^2 \pi^2}{2Ma^2}, \quad 2.$$

where E_g is the semiconductor energy gap and $M = m_e + m_h$ is the exciton translation mass. This case is called the weak confinement regime and, obviously, can be realized in large enough crystals. It has been carefully studied in CuCl nanocrystals where, because $a_B = 7 \text{ \AA}$, the condition $a \gg a_B$ held for all the investigated samples (9–12). Figure 1 shows the evolution of CuCl nanocrystal absorption spectrum with size. These spectra exhibit two exciton lines connected with 2 hole subbands. The lowest hole subband is parabolic, and its size dependence is described very well by Equation 2 (8, 11).

Intermediate Confinement Regime

An interesting situation occurs in semiconductors with very different values of the electron and hole effective masses in an intermediate region of sizes $a_e > a > a_h$, where $a_e = \kappa \hbar^2 / m_e e^2$ and $a_h = \kappa \hbar^2 / m_h e^2$ are the Bohr radii of electrons and holes, respectively. In this case, the hole moves in the average potential of the much faster electron and is localized at the center of the nanocrystal. The region of the hole motion around the crystal center in this case is much smaller than the nanocrystal radius and the size dependence of the exciton ground state can then be described as the behavior of a donor localized at the nanocrystal center. The excitation spectrum of such a donor-like exciton can be described as oscillation of the hole about the crystal center. This donor-like exciton has been observed in the absorption spectra of moderate size CdS and CuBr nanocrystals (13–15). Figure 2 shows the size dependence of two exciton lines in CuBr nanocrystals, where the bulk electron Bohr radius is 18 \AA .

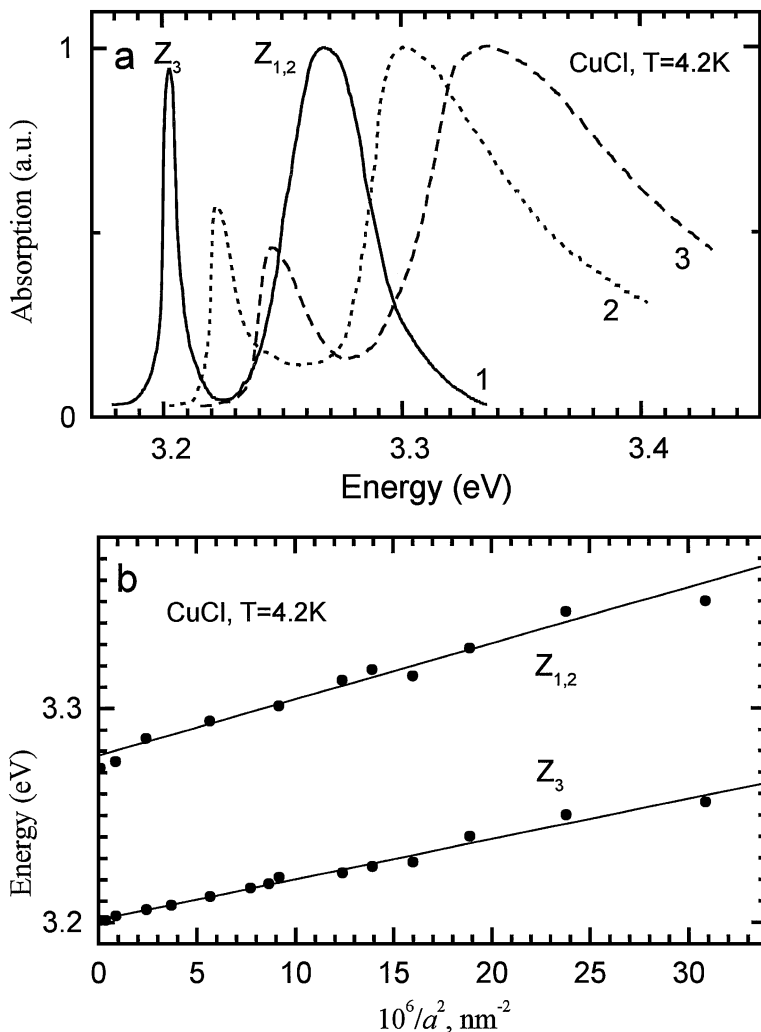


Figure 1 (a) Absorption spectra of CuCl nanocrystals with radius $a = 310$ (1), 29 (2), and 20 (3) Å. (b) Size dependence of the exciton line peak position as function of $1/a^2$, solid lines are theory (11).

Strong Confinement Regime

This case is realized in the small nanocrystals, where $a \ll a_B$. For these nanocrystals, the optical spectra can be considered as spectra of transitions between electron and hole QSLs; the electron-hole Coulomb interaction lowers the energy of these transitions only slightly. The selection rules governing the interband transitions between quantum-size levels of parabolic conduction and valence bands are very

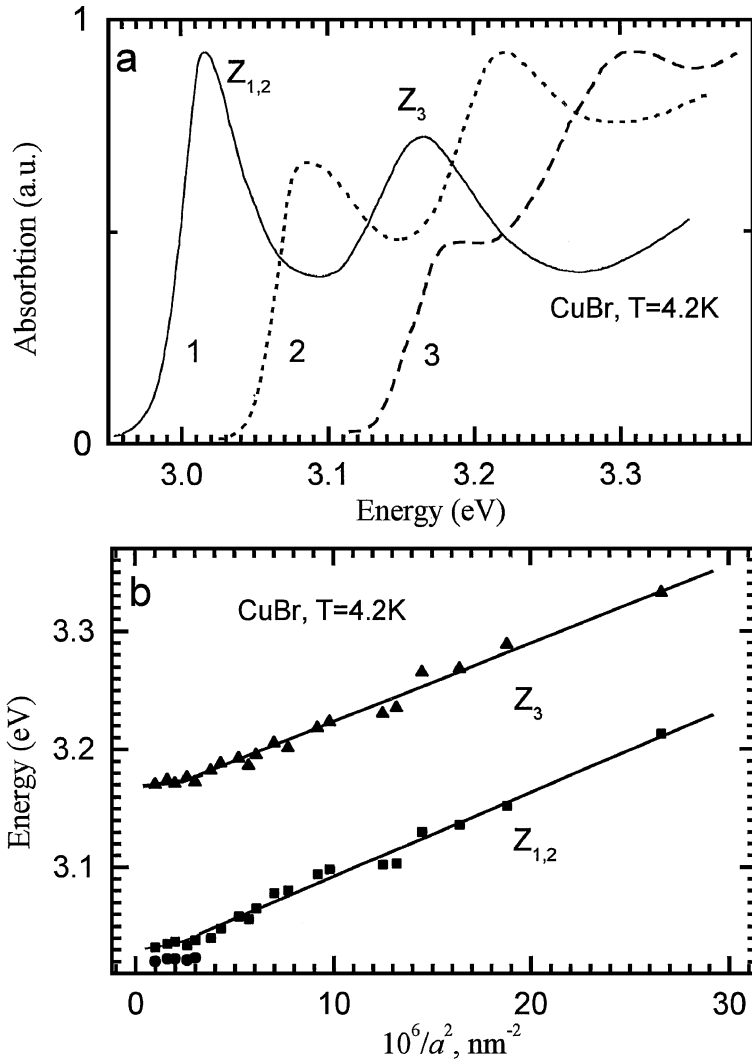


Figure 2 (a) Absorption spectra of CuBr nanocrystals with radius $a = 240$ (1), 36 (2), and 23 (3) Å. (b) Size dependence of the exciton line peak position as function of $1/a^2$; solid lines are theoretical results for a donor-like exciton (14).

simple: Transitions are allowed only between levels with the same quantum numbers. As a result, absorption spectra are given by (7)

$$\hbar\omega_v = E_g + E_v^h(a) + E_v^e(a) - 1.8 \frac{e^2}{\kappa a}, \quad 3.$$

where the Coulomb correction is calculated in first order perturbation theory.

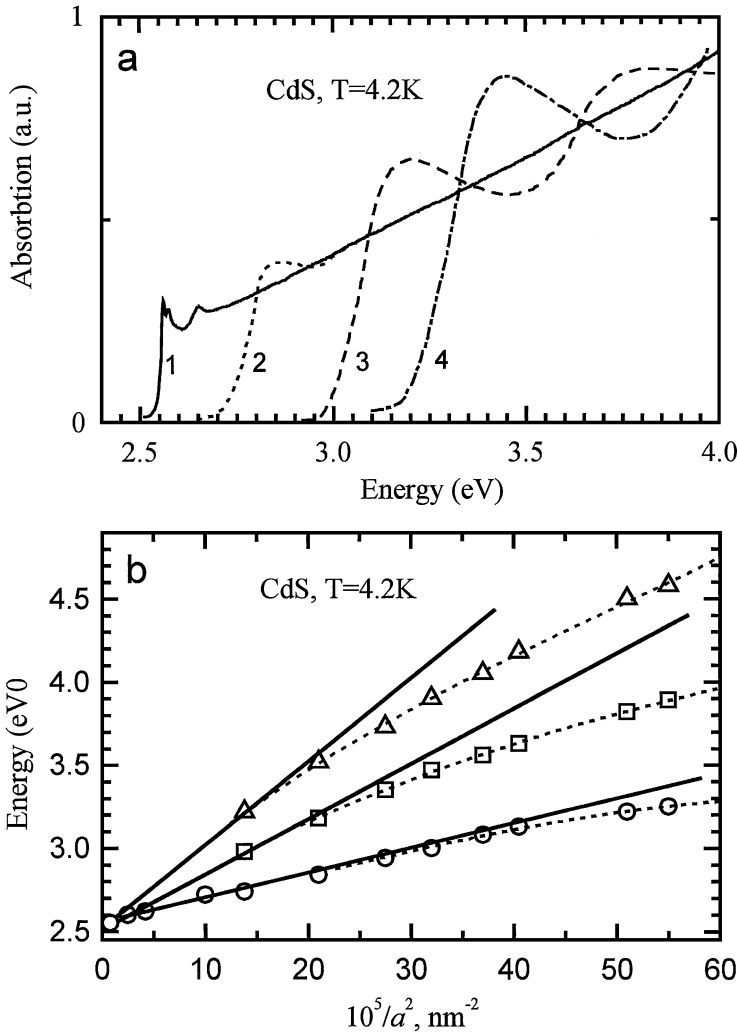


Figure 3 (a) Absorption spectra of CdS nanocrystals with radius $a = 330$ (1), 33 (2), 15 (3) and 12 (4) Å. (b) Size dependence of the exciton line peak position as function of $1/a^2$. Solid lines are results of parabolic band approximation theory (16).

Figure 3 shows the first observed absorption spectra and their size dependence (16) seen in CdS nanocrystals. For the remainder of this review we consider only the case of strong confinement.

Multiband Effective Mass Approximation

Equation 3 looks very simple. There are, however, no semiconductors having simple parabolic conduction and valence bands such as this. Figure 4 shows the

band structure typical of semiconductors having cubic or zinc blende lattice symmetry, e.g. GaAs, InAs, CdSe, CdTe, CdS, and InSb. The conduction band is parabolic only at the bottom of the band. The top of the valence band consists of a 4-fold degenerate sub-band, Γ_8 , describing the dispersion of the light and heavy hole branches for non-zero k , and the spin-orbit split off sub-band Γ_7 . The simple parabolic band approximation is useful only for obtaining a qualitative understanding, not for a quantitative description, of the optical properties of real semiconductors. The optical properties of small nanocrystals arise from transitions between the QSLs of electrons and holes, but in calculating the energies of these levels we must take into account the real band structure found in these semiconductors.

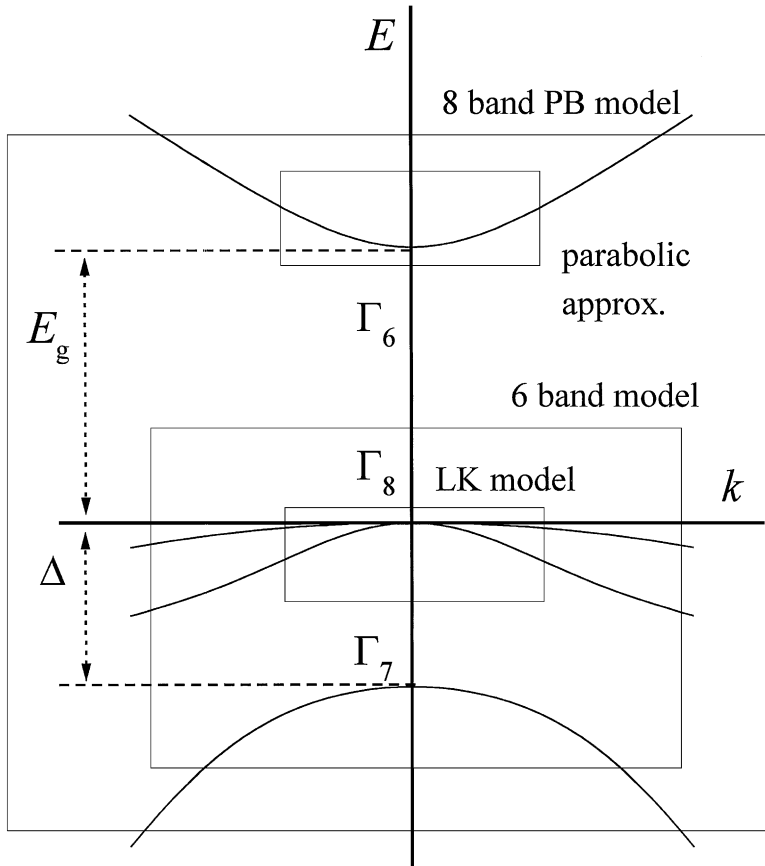


Figure 4 The bulk band structure of a typical direct gap semiconductor with cubic or zinc blende lattice structure and band edge at the Γ -point of the Brillouin zone. The boxes show the region of applicability of the various models used for the calculation of electron and hole QSLs.

If one is interested in the behavior of holes near only the top of the valence band, then the Luttinger & Kohn model (LK) (17) is adequate. In spherical approximation this model contains only two parameters, γ_1^L and γ^L , which determine the effective masses of the light, $m_{lh} = m_0/(\gamma_1^L + 2\gamma^L)$, and heavy, $m_{hh} = m_0/(\gamma_1^L - 2\gamma^L)$, holes, respectively, where m_0 is the free electron mass. Hole levels were calculated within this model (11, 18). However, excited hole levels are not adequately described by this model, and we have to take into account all 3-hole bands: the so called 6-band model. Using the hole levels calculated within this latter model (19), the excitation spectra of CdSe nanocrystals obtained from absorption (20), hole burning (21), and photoluminescence excitation experiments (22–24) were well described. The 6-band model, however, does not take coupling between the conduction and valence bands into account but rather considers the confined electron and hole levels as independent of each other. Intuition and experiment would suggest that this is a good approach for wide-gap semiconductors such as CdSe and CdS, but certainly would not be appropriate for narrow-gap semiconductors where the conduction and valence bands are strongly coupled. A multiband effective mass approximation appropriate for narrow-gap semiconductors was proposed by Pidgeon & Brown (PB) (25) to describe Landau levels in InSb and was successfully used in all other zinc blende semiconductors (see, for example, 26). This 8-band model, which simultaneously takes into account the nonparabolicity of the electron and light hole band dispersion and the complex structure of the valence band, describes the energy band structure in the vicinity of the Γ -point of the Brillouin zone (see Figure 1). The importance of this model for the lowest symmetry QSLs in spherical nanocrystals was also shown by Sercel & Vahala (27, 28). Similar calculations for cubic semiconductors, which have their band edge at the L -point of the Brillouin zone, were carried out by Kang & Wise (29). Recently, general equations for size dependence of electron and hole QSLs within the PB model were developed (30) and were successfully applied to describe narrow gap InAs nanocrystals (31).

THE SPECTROSCOPY OF QUANTUM SIZE LEVELS

General Considerations

In this section we present a theoretical study of the quantum-size level structure of spherical nanocrystals of zinc blende semiconductors within the multiband effective mass approximation. We derive general expressions for the quantum-size levels within the PB model and show why the wide band gap limit of this theory works in CdSe nanocrystals. We discuss the role of the coupling and finally show how this theory, developed for narrow-gap semiconductors, works in InAs nanocrystals.

We calculate the positions of the QSLs assuming that the crystals are spherical and neglecting the warping of the valence band connected with the cubic symmetry

of the zinc blende semiconductor lattice structure. The 8-band Luttinger-Kohn Hamiltonian, which describes the electron and hole motion inside the nanocrystal, has the following form in spherical approximation (25):

	$u_{1/2}^c$	$u_{-1/2}^c$	$u_{3/2,3/2}^v$	$u_{3/2,1/2}^v$	$u_{3/2,-1/2}^v$	$u_{3/2,-3/2}^v$	$u_{1/2,1/2}^v$	$u_{1/2,-1/2}^v$
$u_{1/2}^c$	$E_g + \frac{\alpha}{2m_0} p^2$	0	$\frac{i}{\sqrt{2}} V p_+$	$\sqrt{\frac{2}{3}} V p_z$	$\frac{i}{\sqrt{6}} V p_-$	0	$\frac{i}{\sqrt{3}} V p_z$	$\frac{1}{\sqrt{3}} V p_-$
$u_{-1/2}^c$	0	$E_g + \frac{\alpha}{2m_0} p^2$	0	$-\frac{1}{\sqrt{6}} V p_+$	$i\sqrt{\frac{2}{3}} V p_z$	$-\frac{1}{\sqrt{2}} V p_-$	$\frac{i}{\sqrt{3}} V p_+$	$-\frac{1}{\sqrt{3}} V p_z$
$u_{3/2,3/2}^v$	$-\frac{i}{\sqrt{2}} V p_-$	0	$-(P+Q)$	$-L$	$-M$	0	$-i\sqrt{\frac{1}{2}} L$	$i\sqrt{2} M$
$u_{3/2,1/2}^v$	$\sqrt{\frac{2}{3}} V p_z$	$-\frac{1}{\sqrt{6}} V p_-$	$-L^*$	$-(P-Q)$	0	$-M$	$i\sqrt{2} Q$	$-i\sqrt{\frac{3}{2}} L$
$u_{3/2,-1/2}^v$	$-\frac{i}{\sqrt{6}} V p_+$	$-i\sqrt{\frac{2}{3}} V p_z$	$-M^*$	0	$-(P-Q)$	L	$i\sqrt{\frac{3}{2}} L^*$	$i\sqrt{2} Q$
$u_{3/2,-3/2}^v$	0	$-\frac{1}{\sqrt{2}} V p_+$	0	$-M^*$	L^*	$-(P+Q)$	$i\sqrt{2} M^*$	$i\sqrt{\frac{1}{2}} L^*$
$u_{1/2,1/2}^v$	$-\frac{i}{\sqrt{3}} V p_z$	$-\frac{i}{\sqrt{3}} V p_-$	$i\sqrt{\frac{1}{2}} L^*$	$-i\sqrt{2} Q$	$-i\sqrt{\frac{3}{2}} L$	$-i\sqrt{2} M$	$-\Delta - P$	0
$u_{1/2,-1/2}^v$	$\frac{1}{\sqrt{3}} V p_+$	$-\frac{1}{\sqrt{3}} V p_z$	$-i\sqrt{2} M^*$	$i\sqrt{\frac{3}{2}} L^*$	$-i\sqrt{2} Q$	$-i\sqrt{\frac{1}{2}} L$	0	$-\Delta - P$

4.

The operators in the Hamiltonian are expressed in terms of the momentum operators, $p_{x,y,z} = -i\hbar\nabla_{x,y,z}$:

$$\begin{aligned}
 p_{\pm} &= p_x \pm ip_y, \quad p_{\perp}^2 = p_x^2 + p_y^2, \\
 P &= \frac{\gamma_1}{2m_0} p^2, \quad Q = \frac{\gamma}{2m_0} (p_{\perp}^2 - 2p_z^2), \\
 L &= \frac{-i\sqrt{3}\gamma}{m_0} p_z p_-, \quad M = \frac{\sqrt{3}\gamma}{2m_0} p_-^2.
 \end{aligned}$$

5.

This Hamiltonian takes exact account of the coupling between the 6 valence and 2 conduction bands, separated by an energy gap, E_g . The magnitude of the coupling is described by the Kane matrix element $V = -i\langle S|\hat{p}_z|Z\rangle/m_0$, (32) and Δ is the spin-orbit splitting of the valence band. The Bloch functions of the conduction and

valence bands $u_{J,J_z}^{c,v}$, respectively, have the following form (33, 25):

$$\begin{aligned}
 u_{1/2}^c &= S\uparrow, & u_{3/2,-3/2}^v &= \frac{i}{\sqrt{2}}(X - iY)\downarrow, \\
 u_{-1/2}^c &= S\downarrow, & u_{3/2,3/2}^v &= \frac{1}{\sqrt{2}}(X + iY)\uparrow, \\
 u_{3/2,1/2}^v &= \frac{i}{\sqrt{6}}[(X + iY)\downarrow - 2Z\uparrow], \\
 u_{3/2,-1/2}^v &= \frac{1}{\sqrt{6}}[(X - iY)\uparrow + 2Z\downarrow], \\
 u_{1/2,1/2}^v &= \frac{1}{\sqrt{3}}[(X + iY)\downarrow + Z\uparrow], \\
 u_{1/2,-1/2}^v &= \frac{i}{\sqrt{3}}[-(X - iY)\uparrow + Z\downarrow],
 \end{aligned} \tag{6}$$

where J is the band-edge Bloch function angular momentum (1/2 for the conduction band, 3/2 for the heavy and light hole bands, and 1/2 for the split-off band). The PB Hamiltonian takes into account the contribution of the remote bands to the effective masses of the electrons and holes to second order in perturbation theory. The parameter $\alpha = 1 + 2f$ includes a piece, $2f$, of the contribution to the electron effective mass. The inverse of the electron effective mass, m_e , at the bottom of the conduction band includes this contribution and also a contribution from the valence band, which is expressed in terms of the Kane matrix element and the energy gap (26)

$$\frac{1}{m_e} = \frac{1}{m_0} \left[\alpha + \frac{E_p}{3} \left(\frac{2}{E_g} + \frac{1}{E_g + \Delta} \right) \right], \tag{7}$$

where $E_p = 2m_0V^2$. The parameters γ_1 and γ account for the contribution of the remote bands to the hole effective masses—the terms L, Q, M and P include these contributions. The Luttinger parameters of the valence band, γ_1^L, γ^L , can similarly be written as the sum of contributions from remote bands and from the conduction band (26)

$$\gamma^L = \gamma + \frac{E_p}{6E_g}, \quad \gamma_1^L = \gamma_1 + \frac{E_p}{3E_g}. \tag{8}$$

Diagonalization of Equation 4 gives the dispersion of the conduction and valence bands. For the heavy hole band, we find:

$$E_{hh}(p) = (\gamma_1 - 2\gamma)E_K, \tag{9}$$

where $E_K = p^2/2m_0$ is the kinetic energy of a free electron. For the spectrum of the other three coupled light hole, spin-orbit hole, and electron bands, the dispersion $E(p)$ is given by the equation

$$\begin{aligned} [E - E_g - \alpha E_K] \{ [E + \gamma_1 E_K + \Delta] [E + (\gamma_1 + 2\gamma) E_K] - 8(\gamma E_K)^2 \} \\ - E_p E_K \left(E + \frac{2\Delta}{3} \right) - E_p (\gamma_1 - 2\gamma) E_K^2 = 0. \end{aligned} \quad 10.$$

If one neglects the contribution of the remote bands to the valence band dispersion ($\gamma = 0, \gamma_1 = 0$), we obtain the dispersion of the light holes and electrons in the Kane model (32):

$$(E - E_g - \alpha E_K)(E + \Delta)E - E_p E_K (E + 2\Delta/3) = 0. \quad 11.$$

If we take $\alpha = 0$, then for $E < 0$ Equation 10 gives the dispersion of the light, heavy, and spin-orbit split off hole bands in wide band semiconductors but includes nonparabolicity of the hole bands (see for comparison 19)

$$[E + \gamma_1^L(E) E_K + \Delta] [E + (\gamma_1^L(E) + 2\gamma^L(E)) E_K] - 8(\gamma^L(E) E_K)^2 = 0, \quad 12.$$

where here

$$\gamma^L(E) = \gamma + \frac{E_p}{6(E_g - E)}, \quad \gamma_1^L(E) = \gamma_1 + \frac{E_p}{3(E_g - E)} \quad 13.$$

(see for comparison Equation 8).

The Hamiltonian Equation 4 describes the electron and hole energy spectra only if their typical energies are close enough to the bottom of the conduction band and to the top of the valence band. In practice this means that the quantization energy must be smaller than the distance in energy to the next higher (lower) energy extremum in the conduction (valence) band.

In spherical nanocrystals each electron and hole state is characterized by its parity (\pm), total angular momentum $j = J + L$, where L is the envelope angular momentum, and the projection of the total angular momentum $m = j_z$. The wave functions of these states can be written as a linear expansion in the eight Bloch functions:

$$\begin{aligned} \psi_{j,m}^{\pm}(\mathbf{r}) = R_c(r)^{\pm} \sum_{\mu=-1/2}^{1/2} \Omega_{\mu}^c u_{\mu}^c + \sum_{i=1,2} R_{hi}^{\pm}(r) \\ \times \sum_{\mu=-3/2}^{3/2} \Omega_{\mu}^{hi} u_{3/2,\mu}^v + R_s(r)^{\pm} \sum_{\mu=-1/2}^{1/2} \Omega_{\mu}^s u_{1/2,\mu}^v. \end{aligned} \quad 14.$$

An explicit analytical representation of the angular Ω functions is given in Reference 34. For the even states,

$$\Omega^c = \begin{pmatrix} \sqrt{\frac{j+m}{2j}} Y_{j-1/2, m-1/2} \\ \sqrt{\frac{j-m}{2j}} Y_{j-1/2, m+1/2} \end{pmatrix}, \quad 15.$$

$$\Omega^{h1} = N_1 \begin{bmatrix} \sqrt{3(j+m)(j-m+1)(j-m+2)} Y_{j+1/2, m-3/2} \\ i(j+3m)\sqrt{(j-m+1)} Y_{j+1/2, m-1/2} \\ (j-3m)\sqrt{(j+m+1)} Y_{j+1/2, m+1/2} \\ i\sqrt{3(j-m)(j+m+1)(j+m+2)} Y_{j+1/2, m+3/2} \end{bmatrix},$$

$$\Omega^{h2} = N_2 \begin{bmatrix} -\sqrt{(j+m)(j+m-1)(j+m-2)} Y_{j-3/2, m-3/2} \\ i\sqrt{3(j-m)(j+m-1)(j+m)} Y_{j-3/2, m-1/2} \\ \sqrt{3(j+m)(j-m)(j-m-1)} Y_{j-3/2, m+1/2} \\ -i\sqrt{(j-m)(j-m-1)(j-m-2)} Y_{j-3/2, m+3/2} \end{bmatrix},$$

$$\Omega^s = \begin{bmatrix} \sqrt{\frac{j-m+1}{2(j+1)}} Y_{j+1/2, m-1/2} \\ -i\sqrt{\frac{j+m+1}{2(j+1)}} Y_{j+1/2, m+1/2} \end{bmatrix}, \quad 16.$$

where $N_1 = 1/\sqrt{2j(2j+2)(2j+3)}$, $N_2 = 1/\sqrt{2j(2j-1)(2j-2)}$, and the $Y_{l,m}(\theta, \varphi)$ are the spherical harmonic function as defined in Reference 35. [Note—using alternative definitions of $Y_{l,m}(\theta, \varphi)$ and Bloch functions leads to alternative expressions for the wave function.] Substituting these functions into Equation 4, we obtain four coupled second-order differential equations for the radial functions $R_{c,h1,h2,s}^+(r)$ of the even states:

$$\begin{aligned} & [\varepsilon_g - \varepsilon - \alpha \Delta_{j-1/2}] R_c^+ + \frac{\nu}{\sqrt{6}} \sqrt{1 + 3\eta_j^+} A_{j+1/2}^- R_{h1}^+ \\ & - \frac{\nu}{\sqrt{2}} \sqrt{1 - \eta_j^+} A_{j-3/2}^+ R_{h2}^+ + \frac{\nu}{\sqrt{3}} A_{j+1/2}^- R_s^+ = 0 \\ & \frac{\nu}{\sqrt{6}} \sqrt{1 + 3\eta_j^+} A_{j-1/2}^+ R_c^+ + [\gamma_1 - \gamma(1 - 3\eta_j^+)] \Delta_{j+1/2} - \varepsilon] R_{h1}^+ \\ & + \gamma \sqrt{3(1 + 2\eta_j^+ - 3(\eta_j^+)^2)} A_{j-3/2}^{+2} R_{h2}^+ + \gamma \sqrt{2(1 + 3\eta_j^+)} \Delta_{j+1/2} R_s^+ = 0 \\ & - \frac{\nu}{\sqrt{2}} \sqrt{1 - \eta_j^+} A_{j-1/2}^- R_c^+ + \gamma \sqrt{3(1 + 2\eta_j^+ - 3(\eta_j^+)^2)} A_{j+1/2}^{-2} R_{h1}^+ \\ & + [\gamma_1 + \gamma(1 - 3\eta_j^+)] \Delta_{j-3/2} - \varepsilon] R_{h2}^+ + \gamma \sqrt{6(1 - \eta_j^+)} A_{j+1/2}^{-2} R_s^+ = 0 \end{aligned}$$

$$\begin{aligned} \frac{\nu}{\sqrt{3}} A_{j-1/2}^+ R_c^+ + \gamma \sqrt{2(1+3\eta_j^+)} \Delta_{j+1/2} R_{h1}^+ \\ + \gamma \sqrt{6(1-\eta_j^+)} A_{j-3/2}^{+2} R_{h2}^+ + [\gamma_1 \Delta_{j+1/2} - \delta - \varepsilon] R_s^+ = 0, \end{aligned} \quad 17.$$

where $\eta_j^+ = 1/2j$, $\varepsilon_g = 2m_0 E_g / \hbar^2$, $\delta = 2m_0 \Delta / \hbar^2$, $\nu = 2m_0 V / \hbar$, $\varepsilon = 2m_0 E / \hbar^2$, and E is the energy. The operators

$$A_l^+ = -\frac{\partial}{\partial r} + \frac{l}{r}, \quad A_l^- = \frac{\partial}{\partial r} + \frac{l+1}{r}, \quad 18.$$

are raising and lowering operators for spherical Bessel functions, $j_l(r)$: $A_l^+ j_l(r) = j_{l+1}(r)$, and $A_l^- j_l(r) = j_{l-1}(r)$; $A_l^{+2} = A_{l+1}^+ A_l^+$, $A_l^{-2} = A_{l-1}^- A_l^-$, and Δ_l is the laplacian

$$\Delta_l = \frac{\partial^2}{\partial r^2} + \frac{2}{r} \frac{\partial}{\partial r} - \frac{l(l+1)}{r^2}. \quad 19.$$

Correspondingly, for the odd states, the angular wave functions $\Omega^{c,h1,h2,s}$ can be written :

$$\begin{aligned} \Omega^c &= \begin{pmatrix} -\sqrt{\frac{j-m+1}{2j+2}} Y_{j+1/2,m-1/2} \\ \sqrt{\frac{j+m+1}{2j+2}} Y_{j+1/2,m+1/2} \end{pmatrix}, \\ \Omega^{h1} &= N_1 \begin{bmatrix} \sqrt{3(j+m)(j-m+1)(j+m-1)} Y_{j-1/2,m-3/2} \\ -i(j-3m+1)\sqrt{(j+m)} Y_{j-1/2,m-1/2} \\ (j+3m+1)\sqrt{(j-m)} Y_{j-1/2,m+1/2} \\ -i\sqrt{3(j+m+1)(j-m)(j-m-1)} Y_{j-1/2,m+3/2} \end{bmatrix}, \\ \Omega^{h2} &= N_2 \begin{bmatrix} -\sqrt{(j-m+1)(j-m+2)(j-m+3)} Y_{j+3/2,m-3/2} \\ -i\sqrt{3(j+m+1)(j-m+2)(j-m+1)} Y_{j+3/2,m-1/2} \\ \sqrt{3(j-m+1)(j+m+1)(j+m+2)} Y_{j+3/2,m+1/2} \\ i\sqrt{(j+m+1)(j+m+2)(j+m+3)} Y_{j+3/2,m+3/2} \end{bmatrix}, \\ \Omega^s &= \begin{pmatrix} \sqrt{\frac{j+m}{2j}} Y_{j-1/2,m-1/2} \\ i\sqrt{\frac{j-m}{2j}} Y_{j-1/2,m+1/2} \end{pmatrix}, \end{aligned} \quad 20.$$

where $N_1 = 1/\sqrt{2j(2j+2)(2j-1)}$ and $N_2 = 1/\sqrt{2(j+1)(2j+3)(2j+4)}$.

Substituting these functions into Equation 4, we obtain four coupled second-order differential equations for the radial functions $R_{c,h1,h2,s}^-(r)$ of the odd states:

$$\begin{aligned}
 & [\varepsilon_g - \varepsilon - \alpha \Delta_{j+1/2}] R_c^- - \frac{\nu}{\sqrt{6}} \sqrt{1 - 3\eta_j^-} A_{j-1/2}^+ R_{h1}^- \\
 & + \frac{\nu}{\sqrt{2}} \sqrt{1 + \eta_j^-} A_{j+3/2}^- R_{h2}^- + \frac{\nu}{\sqrt{3}} A_{j-1/2}^+ R_s^- = 0 \\
 & - \frac{\nu}{\sqrt{6}} \sqrt{1 - 3\eta_j^-} A_{j+1/2}^- R_c^- + [\gamma_1 - \gamma(1 + 3\eta_j^-)] \Delta_{j-1/2} - \varepsilon] R_{h1}^- \\
 & + \gamma \sqrt{3[1 - 2\eta_j^- - 3(\eta_j^-)^2]} A_{j+3/2}^- R_{h2}^- - \gamma \sqrt{2(1 - 3\eta_j^-)} \Delta_{j-1/2} R_s^- = 0 \\
 & \frac{\nu}{\sqrt{2}} \sqrt{1 + \eta_j^-} A_{j+1/2}^+ R_c^- + \gamma \sqrt{3[1 - 2\eta_j^- - 3(\eta_j^-)^2]} A_{j-1/2}^+ R_{h1}^- \\
 & + [[\gamma_1 + \gamma(1 + 3\eta_j^-)] \Delta_{j+3/2} - \varepsilon] R_{h2}^- - \gamma \sqrt{6(1 + \eta_j^-)} A_{j-1/2}^+ R_s^- = 0 \\
 & \frac{\nu}{\sqrt{3}} A_{j+1/2}^- R_c^- - \gamma \sqrt{2(1 - 3\eta_j^-)} \Delta_{j-1/2} R_{h1}^- - \gamma \sqrt{6(1 + \eta_j^-)} A_{j+3/2}^- R_{h2}^- \\
 & + [\gamma_1 \Delta_{j-1/2} - \delta - \varepsilon] R_s^- = 0,
 \end{aligned} \tag{21}$$

where $\eta_j^- = 1/(2j + 2)$. In each set (Equations 17 and 21), three of the equations, for the radial functions $R_{h1,h2,s}$ connected with the valence band, are similar to those obtained for the valence band states in the 6-band model (19). The additional equation describes the direct coupling between the conduction and the valence bands.

For convenience, we use the standard atomic notation for the electron and hole QSLs, which are solutions of Equations 17 and 21: nQ_j where j is the total angular momentum, $Q = S, P, D, \dots$ is the spectroscopic notation for the lowest value of L occurring in the equations for the wave functions (described by Equations 15 and 20), and n is the ordinal number of the level with a given symmetry (20). The interband selection rules follow from the properties of the angular wave functions. The only allowed transitions are from $nS_j(h)$ hole states to all $S_{j'}(e)$ electron states, from $nP_j(h)$ hole states to all $P_{j'}(e)$ electron states, etc.

Assuming that the wave functions of all states vanish at the crystal surface gives analytical expressions for the energies of the quantum-size levels in direct gap semiconductors (30). Below, we show what these expressions reduce to in wide-gap CdSe nanocrystals, where the coupling of the conduction and valence bands is not important. Then we discuss the effect of the coupling and show how well the general theory works for narrow-gap InAs nanocrystals.

Wide-Gap Semiconductors: Spectroscopy of CdSe Nanocrystal Quantum-Size Levels

In wide-gap semiconductors one can neglect contributions of the conduction band to the wave functions of the valence band and, conversely, the contributions of the valence bands to the wave function of the conduction band. The equations describing the QSLs of holes can be obtained from the general equations considering the valence band coupling (Equations 31 and 35 of Reference 30) by setting $\alpha = 0$. The equation for the odd hole quantum size levels is

$$\begin{aligned} & -(2j-1)\varepsilon^-(1/k_-^2 - 1/k_+^2)j_{j-1/2}(k_+a)j_{j+3/2}(k_ha)j_{j-1/2}(k_-a) + 3(2j+3) \\ & \times \left[\frac{[\gamma_1(\varepsilon) + 2\gamma(\varepsilon)]k_+^2 + \varepsilon}{k_+^2} j_{j+3/2}(k_-a)j_{j-1/2}(k_+a)j_{j-1/2}(k_ha) \right. \\ & \left. - \frac{[\gamma_1(\varepsilon) + 2\gamma(\varepsilon)]k_-^2 + \varepsilon}{k_-^2} j_{j+3/2}(k_+a)j_{j-1/2}(k_-a)j_{j-1/2}(k_ha) \right] = 0, \quad 22. \end{aligned}$$

where $j = 1/2, 3/2, \dots$, $k_h^2 = \varepsilon/(\gamma_1 - 2\gamma)$ and k_{\pm}^2 is determined from Equation 12:

$$\begin{aligned} k_{\pm}^2 = & \frac{1}{2(\gamma_1^L(\varepsilon) - 2\gamma^L(\varepsilon))(\gamma_1^L(\varepsilon) + 4\gamma^L(\varepsilon))} [2\varepsilon(\gamma_1^L(\varepsilon) + \gamma^L(\varepsilon)) \\ & + \delta(\gamma_1^L(\varepsilon) + 2\gamma^L(\varepsilon)) \pm \{ [2\varepsilon(\gamma_1^L(\varepsilon) + \gamma^L(\varepsilon)) + \delta(\gamma_1^L(\varepsilon) + 2\gamma^L(\varepsilon))]^2 \\ & - 4\varepsilon(\varepsilon + \delta)(\gamma_1^L(\varepsilon) - 2\gamma^L(\varepsilon))(\gamma_1^L(\varepsilon) + 4\gamma^L(\varepsilon)) \}^{1/2}], \quad 23. \end{aligned}$$

where $\gamma_1^L(\varepsilon) = \gamma_1 + v^2/3(\varepsilon - \varepsilon_g)$ and $\gamma^L(\varepsilon) = \gamma + v^2/6(\varepsilon - \varepsilon_g)$. For the even states we find

$$\begin{aligned} & -(2j+3)\varepsilon^+(1/k_-^2 - 1/k_+^2)j_{j+1/2}(k_+a)j_{j-3/2}(k_ha)j_{j+1/2}(k_-a) - 3(2j-1) \\ & \times \left[\frac{[\gamma_1(\varepsilon^+) + 2\gamma(\varepsilon^+)]k_-^2 + \varepsilon^+}{k_-^2} j_{j+1/2}(k_-a)j_{j-3/2}(k_+a)j_{j+1/2}(k_ha) \right. \\ & \left. - \frac{[\gamma_1(\varepsilon^+) + 2\gamma(\varepsilon^+)]k_+^2 + \varepsilon^+}{k_+^2} j_{j+1/2}(k_+a)j_{j-3/2}(k_-a)j_{j+1/2}(k_ha) \right] = 0, \quad 24. \end{aligned}$$

where $j = 3/2, 5/2, \dots$. If $j = 1/2$ the dispersion equation takes the form

$$j_1(k_+a)j_1(k_-a) = 0. \quad 25.$$

For $\varepsilon < \delta$, when $k_-^2 < 0$, the spherical Bessel functions are functions of a complex argument. Equations 22–25 are similar to these obtained for the hole spectra in the 6-band model (20). They differ, however, in the dependence of the Luttinger parameters γ_1^L and γ^L on the energy E , which takes the nonparabolicity of the light hole band into account.

To uncouple the electron QSLs from the valence band states one must set $\gamma_1 = \gamma = 0$ in the general boundary condition equation in Reference 30, mentioned above. In this case, a single equation gives all the electron states (independent of the spin):

$$j_l(ka) = 0, \quad 26.$$

where the quasi-momentum k is written in terms of the QSL energy, ε , via the Kane model dispersion relation (see Equation 11):

$$k^2 = \varepsilon \left[\alpha + \frac{v^2}{3} \left(\frac{2}{\varepsilon_g + \varepsilon} + \frac{1}{\varepsilon_g + \delta + \varepsilon} \right) \right]^{-1}. \quad 27.$$

The resultant equation for the QSLs is identical to that used in Reference 20.

The size dependence of the lowest electron and hole QSLs of CdSe nanocrystals, calculated within this uncoupled model, are shown in Figure 5. The size dependence is plotted as a function of the inverse radius squared. In parabolic approximation, all level energies should scale linearly. The electron QSLs deviate from a linear dependence because nonparabolicity of the conduction band is taken into account. The structure of the hole levels is rather complicated. The hole ground state in CdSe NCs is an even state with total angular momentum $j = 3/2$, and its wave function includes terms with orbital momenta 0 and 2 (it is a $1S_{3/2}$ state according to our notation). The next state is an odd state with $j = 3/2$; its wave function includes contributions with orbital momentum 1 and 3 (it is a $1P_{3/2}$ state according to our notation). One observes crossing of levels of states with different symmetry and an anticrossing of levels with the same symmetry. There are no selection rules connected with the ordinal quantum number as there are for the simple parabolic bands. Therefore, transitions to the first $1S$ electron level are allowed from any hole QSL, which has mixed s - d -type symmetry, and transitions to the $1P$ electron levels are allowed from any hole state that has p or mixed p - f -type symmetry.

In Figure 6 we compare the results of the theory with experiment in CdSe NCs (20). Here the absorption spectrum and its second derivative for CdSe NCs with mean radii 38, 26, and 21 Å can be seen. The calculated position of allowed transitions and their relative intensities are shown by vertical lines. The inset table identifies these transitions. It is seen that the line positions and transition intensities are in rather good agreement with the experimental data. The best descriptions have been obtained for the values $\gamma_1^L = 2.1$, $\gamma^L = 0.55$. The values of the other energy band parameters used $E_p = 17.5$ eV, $E_g = 1.84$ eV, $\Delta = 0.42$ eV, and $\alpha = -0.18$ have been taken from bulk CdSe.

More impressive agreement between theory and experiment has been obtained in the photoluminescence excitation experiments of Norris & Bawendi (22). Figure 7 shows the transition energies as a function of the energy of the first excited state. This figure summarizes the experimental data taken from 24 samples. Strong and weak transitions are denoted by circles and crosses, respectively.

Figure 5 Theoretical size dependence of the electron and hole levels in CdSe nanocrystals, using the 6 band model. The electron energies are relative to the bottom of the conduction band; the hole energies are measured from the top of the valence band. Only those levels involved in transitions with significant oscillator strength are shown. The *p*-type hole states are indicated by dashed lines.

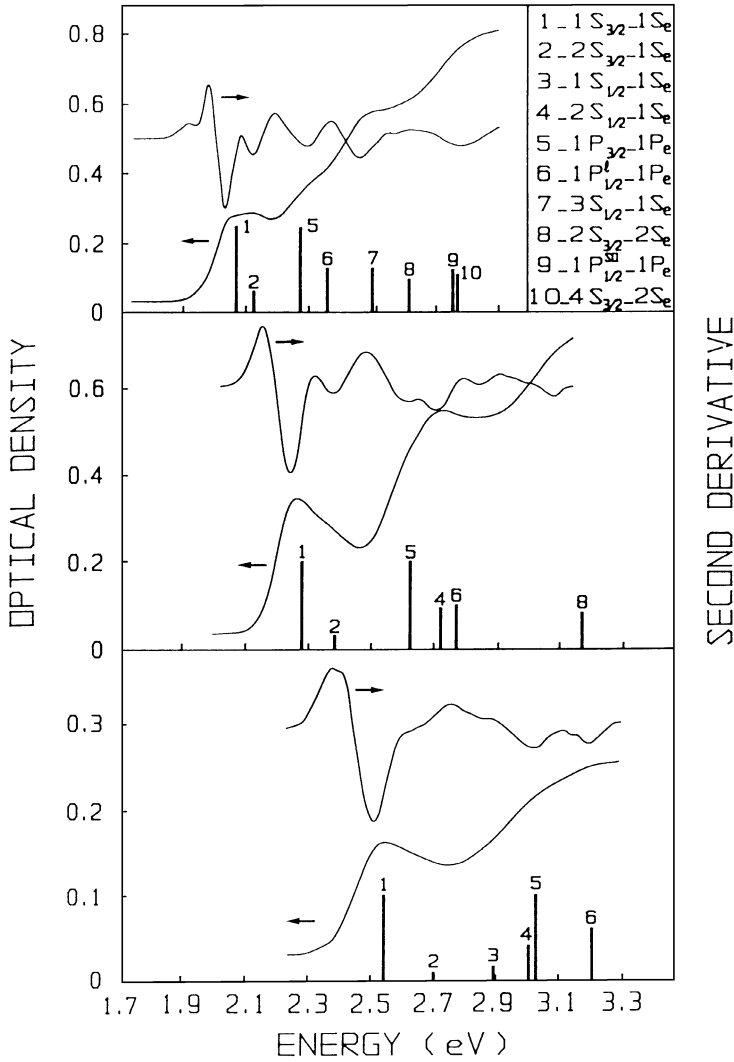


Figure 6 Comparison of the absorption spectra of 38, 26, and 21 Å radius CdSe nanocrystals and their second derivatives with the results of theoretical 6-band calculations. The calculated positions of the transitions are indicated by vertical bars whose height indicates the relative transition strength. The inset shows the assignments of these transitions (20).

The solid and dashed lines are visual guides only to clarify the size evolution. Norris & Bawendi (22) made a detailed comparison of their experimental data with the theory described in Reference 20. Figures 8a and b show the result of this comparison for several of the lowest transitions. The experiment clearly shows the anticrossing of the $1S_{1/2}$, $2S_{1/2}$, and $3S_{1/2}$ levels and that other details of the hole spectra are predicted theoretically.

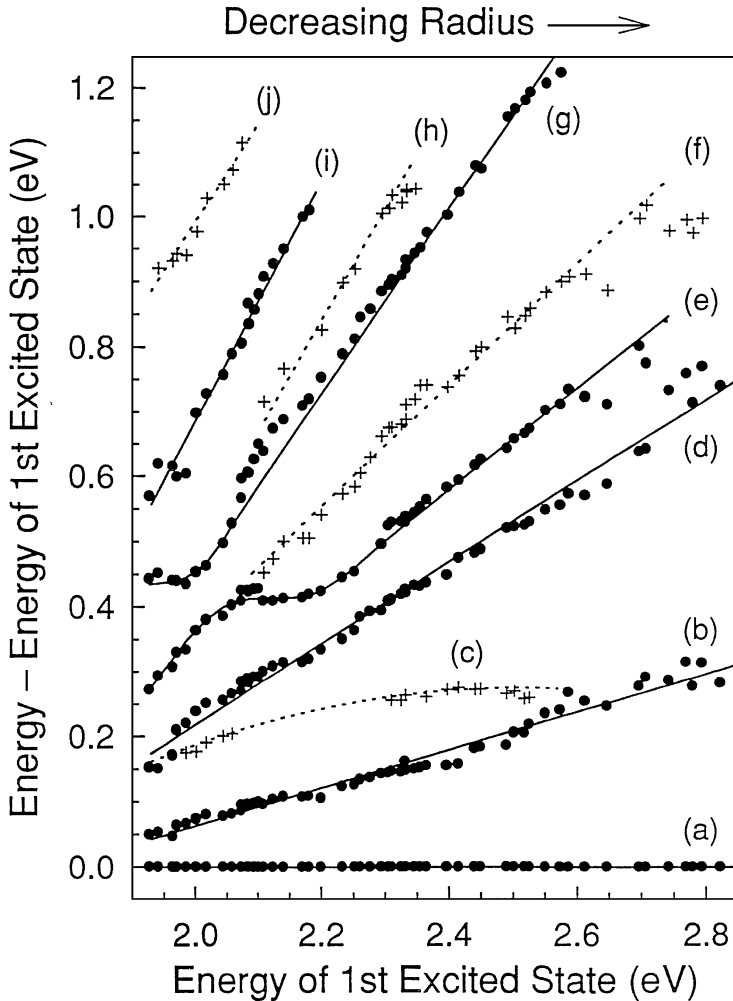


Figure 7 Measured transition energies (relative to the first excited state versus the energy of the first excited state. The plot summarizes data taken from 24 samples. Strong (weak) transitions are denoted by circles (crosses). The solid (dashed) lines are visual guides only for the strong (weak) transitions (22).

Effect of the Band Coupling

The multiband effective mass approximation, which we used for CdSe, considers the confined electron and hole levels independently. This is a reasonable approach for wide-gap semiconductors such as CdSe and CdS, but is not appropriate for narrow-gap semiconductors such as InAs, where the bulk energy gap is only 0.4 eV and where, as a result, the conduction and valence bands are strongly coupled. In

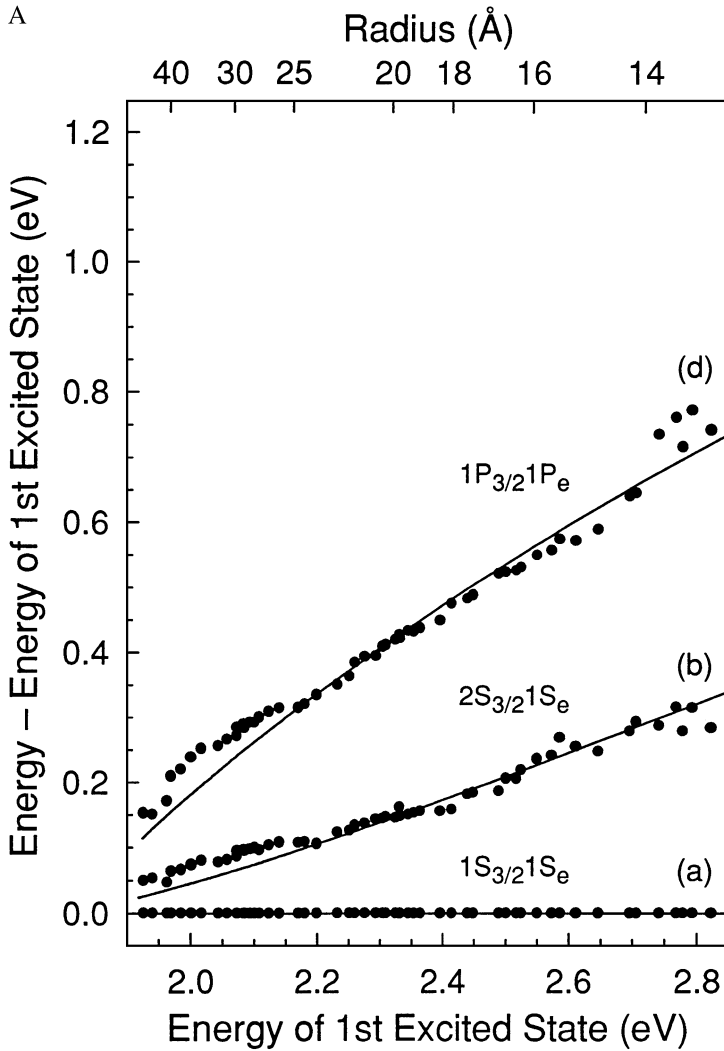


Figure 8 (a) Theoretically predicted pair states (solid lines) assigned to the transitions (a), (b), and (d) in Figure 7; (b) theoretically predicted pair states (solid lines) assigned to the transitions (c), (e), and (g) in Figure 7. The experimental data are shown for comparison (22).

this section we show how the coupling affects the energy levels not only in narrow-gap semiconductors but also in moderate-gap semiconductors.

For simplicity we consider here only the case $\Delta = 0$. The hole levels are twofold degenerate with respect to their spin and are determined by two equations (30):

$$j_{j+1/2}(k_h a) = 0, \quad 28.$$

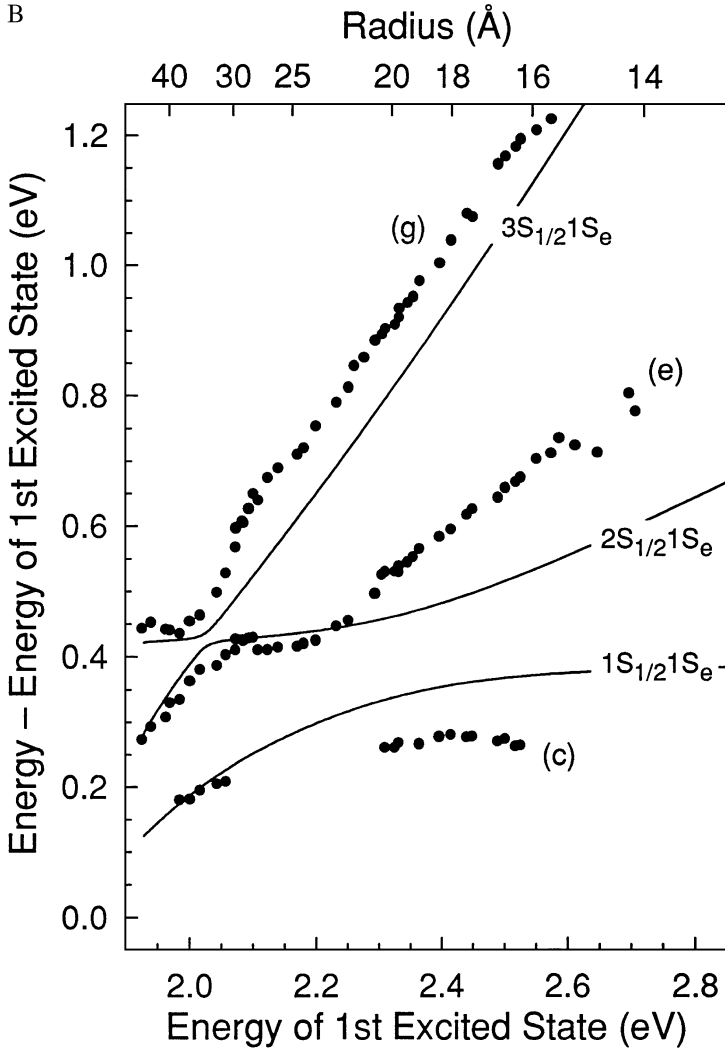


Figure 8 (Continued)

and

$$\begin{aligned}
 & j_{j+1/2}(k_-a)j_{j-3/2}(k_ha) + \frac{1 - \eta_j^+}{1 + \eta_j^+} j_{j+1/2}(k_ha)j_{j-3/2}(k_-a) \\
 &= -\frac{\alpha}{|\alpha|} \sqrt{\frac{\Delta E_h \alpha}{(E_g + \Delta E_h)(\gamma_1 + 4\gamma)}} j_{j-1/2}(k_-a) \\
 &\quad \times \left[j_{j-3/2}(k_ha) - \frac{1 - \eta_j^+}{1 + \eta_j^+} j_{j+1/2}(k_ha) \right],
 \end{aligned}$$

29.

where $j \geq 1/2$ and $E_g = \hbar^2 \varepsilon_g / 2m_0$, and $\Delta E_h = -\hbar^2 \varepsilon / 2m_0$ is the hole level energy measured from the top of the valence band. All hole levels for the case $\Delta = 0$ have a degree of degeneracy greater than 6, except the even state with $j = 1/2$, which is only twofold degenerate. Finite Δ lifts the degeneracy.

It is important to note that the admixture of the conduction band into the valence band is determined not only by the natural energy parameter $\Delta E_h / (E_g + \Delta E_h)$, the ratio of the quantization energy to the energy gap, but also by the ratio $\alpha / (\gamma_1 + 4\gamma)$ (actually the square root of their product). This latter ratio then could produce a large admixture even if the confinement energy were much smaller than the energy gap or, conversely, considerably decrease the admixture even though $\Delta E_h > E_g$.

The electron quantum size levels for $j \geq 1/2$ are described (30):

$$j_{j-1/2}(k_-a) = \frac{1}{2} \frac{\alpha}{|\alpha|} \sqrt{\frac{\Delta E_e (\gamma_1 + 4\gamma)}{(E_g + \Delta E_e) \alpha}} \times [(1 + \eta_j^+) j_{j+1/2}(k_-a) - (1 - \eta_j^+) j_{j-3/2}(k_-a)], \quad 30.$$

where the electron level energies, $\Delta E_e = \hbar^2 (\varepsilon - \varepsilon_g) / 2m_0$, are measured from the bottom of conduction band. All electron levels for $\Delta = 0$, even though they are coupled with the valence band, have the same degree of degeneracy as in the simple parabolic band model [taking electron spin into account, the $1S(e)$ electron level is twofold degenerate, the $1P(e)$ is 6-fold degenerate, etc]. Only finite Δ lifts this degeneracy. As a result the $1P(e)$ electron level is split into $1P_{3/2}(e)$ and $1P_{1/2}(e)$ states.

The admixture of the conduction band into the valence band is determined not only by the natural energy parameter $\Delta E_e / (E_g + \Delta E_e)$, the ratio of the electron quantization energy to the energy gap, but also by $(\gamma_1 + 4\gamma) / \alpha$. This latter parameter can make the admixture large even if the confinement energy is much smaller than the energy gap or can greatly decrease the admixture even if $\Delta E_e > E_g$. The parameter occurring here, however, is the inverse of the one affecting the admixture of the conduction band in the hole levels. So even if the effect of the valence band on the conduction band states is strong, the effect of the conduction band on the hole levels may be weak.

In order to illustrate the role of the coupling, we calculated the size dependence of the lowest hole and electron levels in InP semiconductor nanocrystals using $\Delta = 0$, (this approximation is reasonable because Δ is only 110 meV in InP), and compared these results with calculations done using other techniques. The energy parameters we used are $E_g = 1.424$ eV, $E_p = 20.6$ eV, $f = -1.1$, $\gamma_1^L = 5.25$, and $\gamma^L = (2\gamma_2^L + 3\gamma_3^L) / 5 = 1.9$ (36), which result in $\alpha = -1.2$, $\gamma_1 = 0.41$ and $\gamma = -0.51$. We also calculated the size dependence using another set of values for the parameters $\gamma_1 + 4\gamma$, α , and E_p , now with $\alpha > 0$ and $\gamma_1 + 4\gamma > 0$, but keeping the effective masses of the electron, $m_0(\alpha + E_p/E_g)^{-1}$, light hole, $m_0(\gamma_1 + 4\gamma + E_p/E_g)^{-1}$, and heavy hole, $m_0(\gamma_1 - 2\gamma)^{-1}$, the same as measured in bulk.

In parabolic band approximation the energy of the $1S(e)$ electron level is determined by the simple expression $\Delta E_e = \hbar^2 k_-^2 / 2m_e = \hbar^2 \pi^2 / 2m_e a^2$, where $k_- = \pi/a$ and where $m_e = m_0 / (\alpha + E_p/E_g)$ is the effective mass of the electron at the bottom of the conduction band with $\Delta = 0$ (see Equation 7). In the uncoupled case, ($\gamma_1 = \gamma = 0$), Equation 30 for $j = 1/2$ again gives $k_- = \pi/a$; however, the energy dependence of the effective mass, $m_e(\Delta E_e)$ is taken into account (see Equation 10).

$$\Delta E_e = \frac{\hbar^2 k_-^2}{2m_e(\Delta E_e)} = \frac{\hbar^2 \pi^2}{2m_0 a^2} \left(\alpha + \frac{E_p}{E_g + \Delta E_e} \right). \quad 31.$$

This expression was the one used for the electron QSLs in Reference 20. One sees that the electron effective mass increases with the energy of the levels. Because the position of the level is inversely proportional to the effective mass, the energy dependence of the effective mass slows down the shift of the level with the size (see Figure 3b and 9a). In the full 8-band PB model, k_- is related to the energy in almost the same way as in the Kane model. However, for any finite ΔE_e , when the right side of Equation 30 is nonzero and $\alpha > 0$, the solution of this equation gives $k_- a < \pi$. This leads to a still further slowing down of the size dependence of the electron levels with decreasing size as shown in Figure 9a. If $\alpha < 0$ the root $k_- a$ is greater than π resulting in the shift of the $1S(e)$ electron level to higher energy.

Equations 28 and 29 are for the hole levels for $\Delta = 0$. The first determines the QSLs of heavy holes only and does not couple with the conduction band. The lowest hole level [the $1P_{3/2}(h)$ state] has p -symmetry, and its energy obtained from Equation 28 with $j = 3/2$:

$$\Delta E_h(1P_{3/2}) = \frac{\hbar^2 (4.49)^2}{2m_{hh} a^2}, \quad 32.$$

where $m_{hh} = m_0 / (\gamma_1^L - 2\gamma^L) = m_0 / (\gamma_1 - 2\gamma)$ is the heavy hole effective mass. However, selection rules do not allow optical transitions involving this level and the ground $1S(e)$ electron QSL because of the different symmetries of their envelope wave functions (19, 20).

Hole states with mixed $s - d$ symmetry, for which optical transitions involving the first electron QSL are allowed, are described by Equation 29 with $j = 3/2$. In parabolic approximation and for $\Delta = 0$, their energies are determined by setting the right side of this equation to zero:

$$2j_0(k_h a) j_2(\sqrt{\beta} k_h a) + j_0(\sqrt{\beta} k_h a) j_2(k_h a) = 0, \quad 33.$$

where $k_h^2 = 2m_0 \Delta E_h / [\hbar^2 (\gamma_1^L - 2\gamma^L)]$, $k_-^2 = 2m_0 \Delta E_h / [\hbar^2 (\gamma_1^L + 4\gamma^L)]$, and $\beta = k_-^2 / k_h^2 = (\gamma_1^L - 2\gamma^L) / (\gamma_1^L + 4\gamma^L)$. The values of $k_h a$, which solve this equation, depend only on β . In InP $\beta = 0.115$, and the solution of Equation 33 gives $k_h a \approx 5.21$. The energy of the first hole state with mixed $s - d$ symmetry

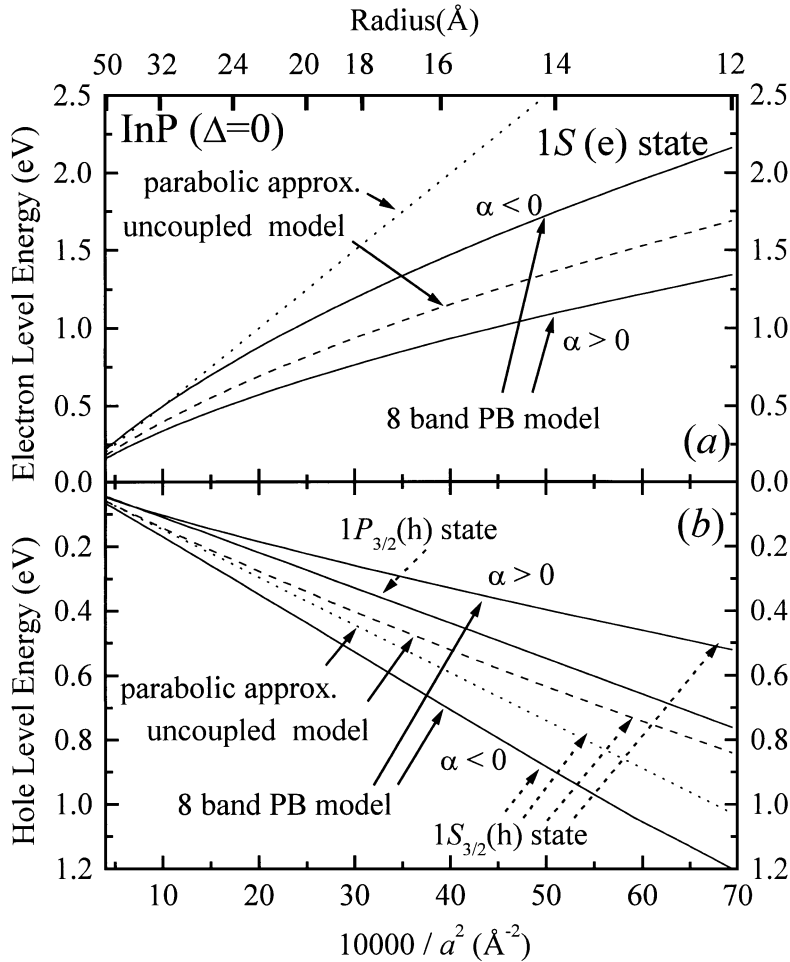


Figure 9 Size dependence of the lowest QSLs in InP nanocrystals, with $\Delta = 0$, calculated using different models: (a) the $1S_e$ electron level and (b) the $1P_{3/2}(h)$ and $1S_{3/2}(h)$ hole levels. Dotted lines show the results of calculations within the simple parabolic approximation for the conduction band and the Luttinger-Kohn parabolic approximation for the valence band. Dashed lines show the effect of the nonparabolicity of the electron and light hole spectra without taking the coupling of the conduction and valence bands into account. Solid lines show the results of the calculations done within the 8-band Pidgeon and Brown model for the set of energy band parameters discussed in the text for $\alpha > 0$ and $\alpha < 0$. The size dependence of the $1P_{3/2}(h)$ hole state is the same for all these models.

(the $1S_{3/2}$ state) when $\Delta = 0$ is then

$$\Delta E_h(1S_{3/2}) = \frac{\hbar^2 k_h^2}{2m_{hh}} = \frac{\hbar^2 (5.21)^2}{2m_{hh} a^2}. \quad 34.$$

Comparison of Equation 32 and Equation 34 shows that the ground hole state in InP nanocrystals has p -type symmetry in parabolic approximation (see also Figure 9b). This level order is consistent with the prediction of the 6-band model for InP nanocrystals (37). Studying the dependence of the solutions of Equation 33 on β shows that for $\Delta = 0$ the level order changes when $\beta > 0.215$ and that the $1S_{3/2}(h)$ state then becomes the ground hole state.

In the uncoupled case, when $\alpha = 0$, the energies of the hole levels are determined by setting the left side of Equation 29 to zero; however, this now takes the nonparabolicity of the light hole into account. The hole energies are then determined by Equation 33 where β is now a function of the energy of the state:

$$\beta(\Delta E_h) = \frac{\gamma_1 - 2\gamma}{\gamma_1^L(\Delta E_h) + 4\gamma^L(\Delta E_h)} = \frac{\gamma_1 - 2\gamma}{\gamma_1 + 4\gamma + E_p/(E_g + \Delta E_h)}. \quad 35.$$

Figure 9b shows that the nonparabolicity of the light hole slows the $1/a^2$ dependence of the $1S_{3/2}(h)$ hole state energies. For holes, if we take coupling with the conduction band into account, for finite $\alpha > 0$ and ΔE_h (when the right hand side of Equation 29 is nonzero and negative) then the solution of this equation gives values of k_a smaller than those found from Equation 33. This leads to a further slowing of the size dependence of the hole levels with decreasing size. Figure 9b shows this dependence for the parameters $\alpha = 0.63$, $\gamma_1 = 1.04$, $\gamma = -0.21$, and $E_p = 18.0$, and keeps the effective carrier masses equal to those measured in bulk InP. For these parameters, the $1S_{3/2}(h)$ level crosses the $1P_{3/2}(h)$ level and becomes the ground hole state for nanocrystal radii less than 35 Å. Negative α leads to an increase of k_a and to a ground state that has p -type symmetry. The corresponding results, calculated for energy parameters (36) $\alpha = -1.2$, $\gamma_1 = 0.41$, $\gamma = -0.51$, and $E_p = 20.6$, are also shown in Figure 9b.

The analysis presented above shows how sensitive the absorption spectra are to the energy band parameters. The structure and positions of the quantum-size levels in small nanocrystals are determined not by the values of the effective masses at the extrema of the conduction band and valence bands alone. They strongly depend on the relative contribution of the remote bands and the nearest band. The drastic change of the level structure presented in Figure 8 is obtained by changing E_p only 10%.

Coupling between the conduction and valence bands might also lead to formation of intrinsic gap states in semiconductors (38). These states may play an important role in photoluminescence and absorption of small nanocrystals.

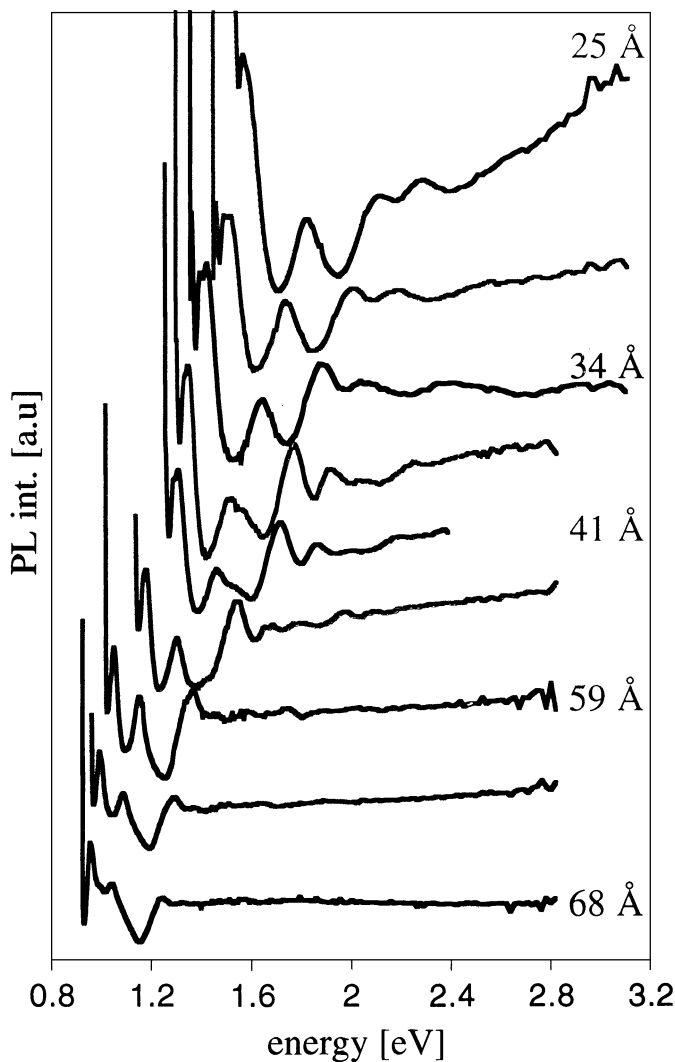


Figure 10 Size-selected PLE spectra for InAs nanocrystals ranging in diameter between 68 and 25 Å ($T = 10$ K) (31).

Narrow Gap Semiconductors: Spectroscopy of InAs Nanocrystal Quantum-size Levels

The 8-band theory of quantum-size levels describes the size dependence of the absorption spectrum of narrow gap InAs nanocrystals. Figure 10 shows the

photoluminescence excitation spectra (PLE) of InAs nanocrystal samples with diameters between 25 and 67 Å (31). The PLE of these samples show as many as nine peaks, corresponding to the transitions between a number of electron and hole QSLs. The energy of these transitions are between 0.8 and 2.4 eV. The bulk energy gap of InAs is only 0.42 eV. This means that the confinement energies of the electrons and holes in this material are larger than the energy gap, and we must explicitly take the coupling between conduction and valence bands into account.

The confined electron and hole states were found by numerically solving Equation 17 and 21 for the radial functions $R^\pm(r)$. We used bulk parameters taken from the literature to describe the band structure of InAs: energy gap $E_g = 0.418$ eV, spin-orbit splitting $\Delta = 0.38$ eV, and gamma parameters $\gamma = 8.9$ and $\gamma_1 = 19.7$ (39); the value of the nonparabolicity parameter, $E_p = 21.6$ eV, was selected to get the measured electron effective mass at the bottom of the conduction band. The nanocrystals studied in the experiment were embedded in a polymer having an optical energy gap 4.5 eV; we modeled the medium surrounding the nanocrystal by using finite 2-eV barriers for both electrons and holes. The other band parameters in the barriers were taken to be the same as in bulk InAs. We used standard atomic notation for electron and hole states: nQ_F . The e - h transition energies were taken as the difference between the electron and hole energies reduced by the first order contribution to pair binding $-1.8e^2/\kappa a$ (7) (~ 170 meV in small crystals), where κ is the bulk dielectric constant. In calculating oscillator strengths, we averaged over all linear polarizations of the dipole transition operator.

Figure 11 shows the energies of higher transitions, measured relative to the $1S_{3/2}(h)1S_{1/2}(e)$ ground state transition energy, as a function of the ground state transition energy. We take the latter as the average of the position of the first PLE peak and the detection window, which is a measure of nanocrystal size and is unambiguously defined and more accurately known than the dot size (31). The *left panel* compares the observed transitions with those calculated within the 8-band model. The *right panel* shows the calculated relative oscillator strengths for the optically active transitions. The calculated level separations closely reproduce the observed strong transitions. The calculated energies of the $2S_{3/2}(h)1S_{1/2}(e)$ and $1S_{1/2}(h)1S_{1/2}(e)$ transitions cross at $E_1 = 1.5$ eV. For large dots the $2S_{3/2}(h)1S_{1/2}(e)$ transition is stronger than the $1S_{1/2}(h)1S_{1/2}(e)$. After the crossing, the $2S_{3/2}(h)1S_{1/2}(e)$ oscillator strength vanishes, while the $1S_{1/2}(h)1S_{1/2}(e)$ oscillator strength increases. The observed PLE peak (crosses in Figure 4) corresponds to one of these transitions for large dots and to the other for small dots. This explains why this PLE peak does not shift for small dots. The strong transition E_5 follows both the $1P_{3/2}(h)1P_{1/2}(e)$ and $1P_{3/2}(h)1P_{3/2}(e)$ transitions very well. One consequence of the PB model is the splitting of the 6-fold degenerate $1P_e$ electron level (taking electron spin projection into account) into $1P_{1/2}(e)$ and $1P_{3/2}(e)$ states as a consequence of strong spin-orbit coupling in the valence band. The next weak E_6 line can be identified as the $2S_{1/2}(h)1S_{1/2}(e)$ transition. It appears to merge into the next higher strong E_7 transition. This correlates well with

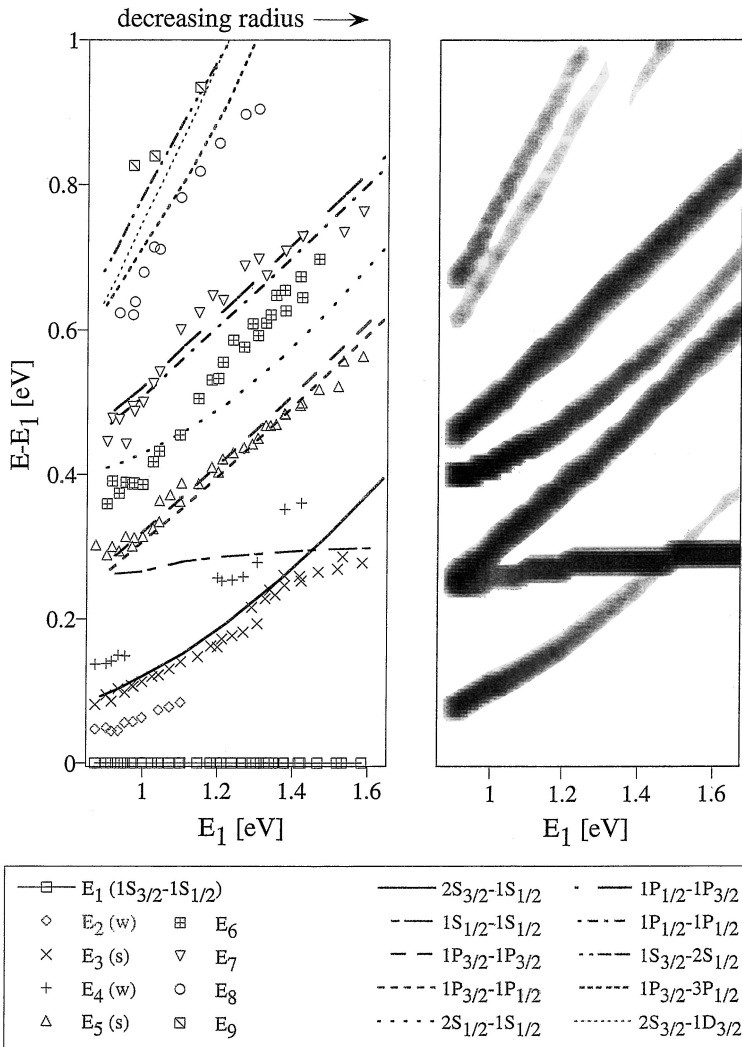


Figure 11 Map of the levels for InAs nanocrystals extracted from the PLE experiments. Transition energies relative to the lowest transition are plotted versus the energy of the lowest transition. *Left panel*: The experimental results are compared with the levels calculated using the PB model. *Right panel*: Calculated oscillator strengths, represented by relative darkness, for the transitions in the left frame (31).

the decrease of the oscillator strength of the $2S_{1/2}(h)1S_{1/2}(e)$ transition in small crystals. The discrepancy of the E_6 line from the calculated dependence is probably due to the neglect of the Coulomb mixing of $e-h$ pair states with the same total angular momentum, which leads to a repulsion between the $1P_{3/2}(h)1P_{3/2}(e)$ and $2S_{1/2}(h)1S_{1/2}(e)$ exciton states and shifts the latter to higher energy. The E_7 line is

described very well by the $1P_{1/2}(h)1P_{1/2}(e)$ and $1P_{1/2}(h)1P_{3/2}(e)$ transitions. The highest, weakly excited states are ascribed to a combination of several transitions listed in the *lower panel*.

The successful description of the level separations and their relative transition intensities by the PB model seen in Figure 10 raises this question, Why is there a discrepancy in the description of the size dependence of the ground state transition in the smallest nanocrystals (31)? If the discrepancy reflects a deviation of the energy band structure from the PB model and/or an underestimation of the electron wave function penetration into the barrier, then it should increase for higher transitions and we should not be able to describe the level separation, e.g. between the $1P_{3/2}(h)1P_{1/2}(e)$ and $1S_{3/2}(h)1S_{1/2}(e)$ ground state transition. A similar effect has been observed in CdSe nanocrystals where the theory does not reproduce the curvature of the size dependence of the ground state transition, yet it reproduces the level separations for most transitions as a function of the ground state transition energy very well (22). The size dependence of the absorption spectra can be fit if we use some measure of dot size that yields radii larger than those obtained by HRTEM (in the smallest InAs nanocrystals up to 2.5 Å larger). Further experiments studying the effect of the matrix-nanocrystal interface on the level positions are needed to clarify this effect.

Another explanation is the underestimation of the strength of the electron-hole Coulomb interaction in smallest crystals. In References 22 and 31 the dielectric constant was taken as the static dielectric constant of the bulk. However, the coupling with polar optical phonons goes to zero in small nanocrystal (40), and one should replace the static dielectric constant with the high-frequency dielectric constant, which itself decreases with nanocrystal size. There is no self-consistent theory of this effect at present.

Thus a multiband effective mass theory of the quantum-size levels in narrow-gap and wide-gap semiconductor nanocrystals based on the spherical PB model has been developed. Analytical results show that conduction and valence band coupling may be important even in semiconductors with relatively wide gaps. The theory successfully describes the observed level structure and transition intensities of CdSe and InAs nanocrystals and clearly should quantitatively describe the level structure in most tetrahedral direct gap semiconductor nanocrystals.

FINE STRUCTURE OF THE BAND EDGE EXCITON

While the large-scale structure of the absorption spectra as shown above is now fairly well understood, the nature of the emitting state remains controversial. The photoluminescence of high-quality samples with high-quantum yield is red shifted with respect to the excitation frequency and has an unusually long radiative lifetime ($\tau_R \sim 1 \mu s$ at 10 K) (41) compared with the bulk exciton recombination time ($\tau_R \sim 1 ns$). Simple parabolic band theory cannot explain this data in terms of

recombination through internal states, and band edge emission in II-VI QDs was explained early on as a surface effect and attributed to the recombination of weakly overlapping, surface-localized carriers (41, 42).

The results of realistic calculations of the band edge exciton (43) show that intrinsic Dark Exciton states occur, which are responsible for the luminescence and allow one to resolve the puzzle without involving the surface. The existence of such dark states has been confirmed in CdSe (43–46), InP (47), and InAs (48) nanocrystals, as well as in porous Si (49, 50).

We model the CdSe band edge exciton using the parabolic conduction band model and the Luttinger band model for the valence band. In the framework of the parabolic effective mass approximation, for spherically symmetric crystals, i.e. finite size spherical crystals having a cubic lattice structure, the first electron quantum size level is a $1S_e$ state doubly degenerate with respect to its spin projection. The energy of this state is (see Equation 1) $E_{1S} = \frac{\hbar^2 \pi^2}{2m_e a^2}$ and the corresponding wave functions are

$$\psi_\alpha(\mathbf{r}) = \xi(\mathbf{r})|u_\alpha^c\rangle = \sqrt{\frac{2}{a}} \frac{\sin(\pi r/a)}{r} Y_{00}(\Omega) |S\alpha\rangle, \quad 36.$$

where $\alpha = \downarrow (\uparrow)$ is the projection of the electron spin $s_z = -(+)1/2$. As mentioned above, the first hole QSL is a $1S_{3/2}$ state, which is 4-fold degenerate with respect to the projection of its total angular momentum, ($M = 3/2, 1/2, -1/2$, and $-3/2$) (20). For holes in the 4-fold degenerate valence band the energy and wave functions can be written

$$E_{3/2}(\beta) = \frac{\hbar^2 \varphi^2(\beta)}{2m_{hh} a^2}, \quad 37.$$

$$\psi_M(\mathbf{r}) = 2 \sum_{l=0,2} R_l(r) (-1)^{M-3/2} \sum_{m+\mu=M} \begin{pmatrix} 3/2 & l & 3/2 \\ \mu & m & -M \end{pmatrix} Y_{lm}(\Omega) u_{3/2,\mu}^v, \quad 38.$$

where $\beta = m_{lh}/m_{hh}$ is the ratio of the light to heavy hole effective masses, $\begin{pmatrix} i & k & l \\ m & n & p \end{pmatrix}$ are Wigner 3j-symbols, u_μ ($\mu = \pm 1/2, \pm 3/2$) are the Bloch functions defined in Equation 6, and $\varphi(\beta)$ is the first root of the equation (11, 18, 27, 51):

$$j_0(\varphi) j_2(\sqrt{\beta} \varphi) + j_2(\varphi) j_0(\sqrt{\beta} \varphi) = 0, \quad 39.$$

The radial functions $R_l(r)$ are (51, 52):

$$\begin{aligned} R_2(r) &= \frac{A}{a^{3/2}} \left[j_2(\varphi r/a) + \frac{j_0(\varphi)}{j_0(\varphi \sqrt{\beta})} j_2(\varphi \sqrt{\beta} r/a) \right], \\ R_0(r) &= \frac{A}{a^{3/2}} \left[j_0(\varphi r/a) - \frac{j_0(\varphi)}{j_0(\varphi \sqrt{\beta})} j_0(\varphi \sqrt{\beta} r/a) \right], \end{aligned} \quad 40.$$

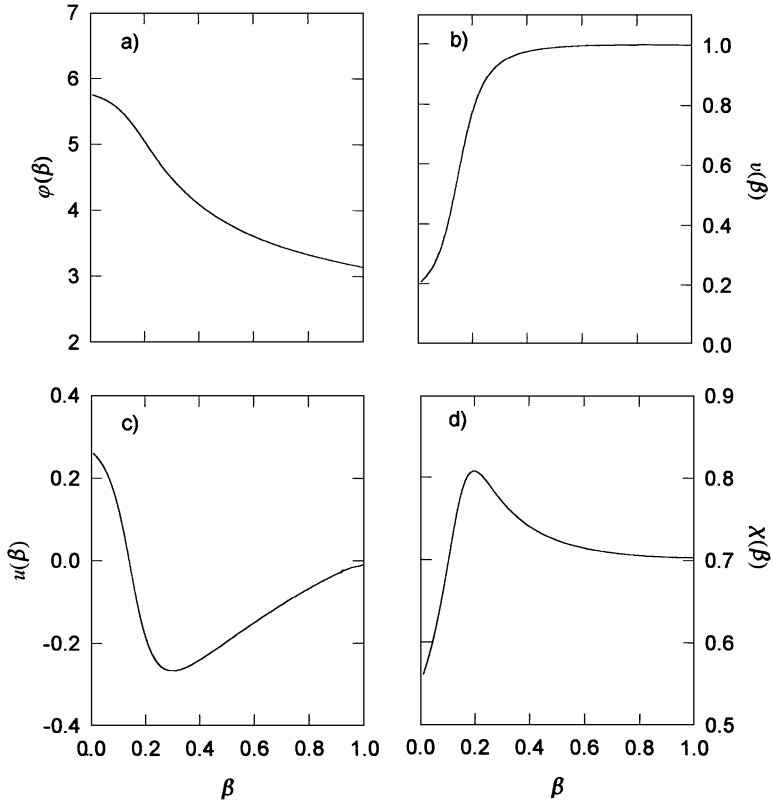


Figure 12 (a) The dependence of the hole ground state function $\varphi(\beta)$ on the light to heavy hole effective mass ratio, β ; (b) the dimensionless function $v(\beta)$ associated with hole level splitting due to hexagonal lattice structure; (c) the dimensionless function $u(\beta)$ associated with hole level splitting due to crystal shape asymmetry; (d) the dimensionless function $\chi(\beta)$ associated with exciton splitting due to the electron-hole exchange interaction (46).

where the constant A is determined by the normalization condition:

$$\int dr r^2 [R_0^2(r) + R_2^2(r)] = 1. \quad 41.$$

The dependence of φ on β (51) is presented in Figure 12a.

For spherical dots the exciton ground state ($1S_{3/2}1S_e$) is 8-fold degenerate. However, shape and internal crystal structure anisotropy together with the electron hole exchange interaction lift this degeneracy. The splitting and the transition oscillator strengths of the states, as well as their order, are very sensitive to crystal size and shape, as shown below. We have calculated this splitting for CdSe nanocrystals, neglecting the warping of the valence band and the nonparabolicity of the electron and light hole energy spectra.

Effect of Intrinsic Crystal Field and Nanocrystal Shape Anisotropy

Nanocrystal asymmetry lifts the hole state degeneracy. The asymmetry has two sources: the intrinsic asymmetry of the hexagonal lattice structure of the crystal (51) and the nonspherical shape of the finite crystal (53). Both split the 4-fold degenerate hole state into two 2-fold degenerate states—a Kramer's doublet having $|M| = 1/2$ and $3/2$, respectively.

The splitting due to the intrinsic hexagonal lattice structure, Δ_{int} , can be written (51):

$$\Delta_{int} = \Delta_{cr} v(\beta), \quad 42.$$

where Δ_{cr} is the crystal field splitting, equal to the distance between the A and B valence subbands in bulk semiconductors having a hexagonal lattice structure (25 meV in CdSe). Equation 42 is obtained within the framework of the quasicubic model and when the crystal field splitting can be considered as a perturbation. The Kramer's doublet splitting does not depend on crystal size but only on the ratio of the light to heavy hole effective masses. The dimensionless function $v(\beta)$ describing this dependence, shown in Figure 12b, varies rapidly in the region $0 < \beta < 0.3$. The $|M| = 3/2$ state is the ground state.

In addition to the intrinsic asymmetry, there is also the asymmetry connected with the non-spherical shape of the nanocrystals. TEM measurements show that small CdSe nanocrystals are slightly prolate or oblate along their hexagonal axis. The non-sphericity of the crystal was modeled by taking it to be an ellipsoid whose deviation from sphericity is characterized by the ratio $c/b = 1 + \mu$ of its major to minor axes. Here μ is the ellipticity of the crystal and is positive (negative) for prolate (oblate) crystals. The splitting arising from this deviation was calculated to first order in perturbation theory (53):

$$\Delta_{sh} = 2\mu u(\beta) E_{3/2}(\beta), \quad 43.$$

where $E_{3/2}$ is the $1S_{3/2}$ hole ground state energy for spherical crystals of radius $a = (b^2 c)^{1/3}$. $E_{3/2}$ is inversely proportional to a^2 (see Equation 37) and the shape splitting is therefore a sensitive function of the crystal size. The function $u(\beta)$ decreases from a value of $4/15$ at $\beta = 0$, changes sign at $\beta = 0.14$ and again goes to zero at $\beta = 1$ (see Figure 12c).

The net splitting of the hole state, $\Delta(a, \beta, \mu)$, is the sum of the crystal field and shape splitting,

$$\Delta(a, \beta, \mu) = \Delta_{sh} + \Delta_{int}. \quad 44.$$

In crystals where the function $u(\beta)$ is negative, e.g. in CdSe crystals where $\beta = 0.28$, the net splitting decreases with size in prolate ($\mu > 0$) crystals. Even the order of the hole levels can change, with the $|M| = 1/2$ state becoming the ground hole level for sufficiently small crystals (LE Brus, unpublished data). This

can be qualitatively understood within the framework of uncoupled A and B valence subbands. In prolate crystals the energy of the lowest hole quantum-size level is determined by its motion in the plane perpendicular to the hexagonal axis. In this plane, the hole effective mass in the lower sub-band, A, is smaller than that in the higher B subband. Decreasing the size of the crystal causes a shift of the quantum-size level that is inversely proportional to both the effective mass and the square of the nanocrystal radius. The shift is therefore larger for the A subband than for the B subband and, as a result, can change the order of the levels in small crystals. In oblate ($\mu < 0$) crystals where the levels are determined by motion along the hexagonal axis, the B subband has the smaller mass. Hence, the net splitting increases with decreasing size and the states maintain their original order.

Exchange Interaction in Nanocrystals

The electron-hole exchange interaction becomes very important in small nanocrystals. This interaction also breaks the 8-fold degeneracy of the spherical band edge exciton and mixes different electron and hole spin states. It has the following form (33, 54):

$$\hat{H}_{exch} = -(2/3)\varepsilon_{exch}(a_0)^3\delta(\mathbf{r}_e - \mathbf{r}_h) \boldsymbol{\sigma} \mathbf{J}, \quad 45.$$

where the $\boldsymbol{\sigma}$ are the electron Pauli spin-1/2 matrices, \mathbf{J} are the hole spin 3/2 matrices, a_0 is the lattice constant, and ε_{exch} is the exchange strength constant. In bulk crystals with cubic lattice structure this term splits the 8-fold degenerate ground exciton state into a 5-fold degenerate optically passive state with total angular momentum 2 and a 3-fold degenerate optically active state with total angular momentum 1. This splitting can be expressed in terms of the bulk exciton Bohr radius, a_{ex} :

$$\hbar\omega_{ST} = (8/3\pi)(a_0/a_{ex})^3\varepsilon_{exch}. \quad 46.$$

In bulk crystals with hexagonal lattice structure this term splits the exciton 4-fold degenerate ground state into a triplet and a singlet state, separated by

$$\hbar\omega_{ST} = (2/\pi)(a_0/a_{ex})^3\varepsilon_{exch}. \quad 47.$$

Equations 46 and 47 allow one to evaluate the exchange strength constant. In CdSe crystals, where $\hbar\omega_{ST} = 0.13$ meV (55), a value of $\varepsilon_{exch} = 450$ meV is obtained using $a_{ex} = 56$ Å.

The contribution of Equation 45 depends on the average distance between the electron and hole, and in small crystals where they are confined, is inversely proportional to the cube of the crystal radius. As a result the magnitude of this term grows tremendously and reaches a value of 10–20 meV in small crystals.

Fine Structure of the Band Edge Exciton

Taken together, the hexagonal lattice structure, crystal shape asymmetry, and the electron-hole exchange interaction split the original spherical 8-fold degenerate

exciton into five levels. The levels are labeled by the magnitude of the projection of the exciton total angular momentum, $F = M + s_z$: one level with $F = \pm 2$, two with $F = \pm 1$, and two with $F = 0$. The level energies, $\varepsilon_{|F|}$, are determined by solving the secular equation $\det(\hat{E} - \varepsilon_{|F|}) = 0$, where the matrix \hat{E} consists of matrix elements between the exciton wave functions $\Psi_{\alpha,M}(\mathbf{r}_e, \mathbf{r}_h) = \psi_{\alpha}(\mathbf{r}_e)\psi_M(\mathbf{r}_h)$ of the asymmetry perturbations and the exchange interaction, \hat{H}_{exch} , (46):

	$\uparrow, 3/2$	$\uparrow, 1/2$	$\uparrow, -1/2$	$\uparrow, -3/2$	$\downarrow, 3/2$	$\downarrow, 1/2$	$\downarrow, -1/2$	$\downarrow, -3/2$
$\uparrow, 3/2$	$\frac{-3\eta}{2} - \frac{\Delta}{2}$	0	0	0	0	0	0	0
$\uparrow, 1/2$	0	$\frac{-\eta}{2} + \frac{\Delta}{2}$	0	0	$-i\sqrt{3}\eta$	0	0	0
$\uparrow, -1/2$	0	0	$\frac{\eta}{2} + \frac{\Delta}{2}$	0	0	$-i2\eta$	0	0
$\uparrow, -3/2$	0	0	0	$\frac{3\eta}{2} - \frac{\Delta}{2}$	0	0	$-i\sqrt{3}\eta$	0
$\downarrow, 3/2$	0	$i\sqrt{3}\eta$	0	0	$\frac{3\eta}{2} - \frac{\Delta}{2}$	0	0	0
$\downarrow, 1/2$	0	0	$i2\eta$	0	0	$\frac{\eta}{2} + \frac{\Delta}{2}$	0	0
$\downarrow, -1/2$	0	0	0	$i\sqrt{3}\eta$	0	0	$\frac{-\eta}{2} + \frac{\Delta}{2}$	0
$\downarrow, -3/2$	0	0	0	0	0	0	0	$\frac{-3\eta}{2} - \frac{\Delta}{2}$

48.

where $\eta = (a_{ex}/a)^3 \hbar \omega_{ST} \chi(\beta)$, and the dimensionless function $\chi(\beta)$ is written in terms of the electron and hole radial wave functions (46),

$$\chi(\beta) = (1/6)a^2 \int_0^a dr \sin^2(\pi r/a) [R_0^2(r) + 0.2R_2^2(r)]. \quad 49.$$

The dependence of χ on the parameter β is shown in Figure 12d.

Solution of the secular equation yields five exciton levels. The energy of the exciton with total angular momentum projection $|F| = 2$ and its dependence on crystal size is given by (46)

$$\varepsilon_2 = -3\eta/2 - \Delta/2. \quad 50.$$

The respective wave functions are

$$\Psi_{-2}(\mathbf{r}_e, \mathbf{r}_h) = \Psi_{\downarrow, -3/2}(\mathbf{r}_e, \mathbf{r}_h), \quad \Psi_2(\mathbf{r}_e, \mathbf{r}_h) = \Psi_{\uparrow, 3/2}(\mathbf{r}_e, \mathbf{r}_h). \quad 51.$$

The energies and size dependence of the two levels, each with total momentum projection $|F| = 1$, are given by

$$\varepsilon_1^{U,L} = \eta/2 \pm \sqrt{(2\eta - \Delta)^2/4 + 3\eta^2}, \quad 52.$$

where U and L correspond to the upper (“+” in this equation) and lower (“−” in this equation) sign respectively. We denote these states by $\pm 1^U$ and $\pm 1^L$, respectively; i.e. the upper and lower state with projection $F = \pm 1$. The corresponding wave functions for the states with $F = +1$ are

$$\Psi_1^{U,L}(\mathbf{r}_e, \mathbf{r}_h) = \mp i C^+ \Psi_{\uparrow, 1/2}(\mathbf{r}_e, \mathbf{r}_h) + C^- \Psi_{\downarrow, 3/2}(\mathbf{r}_e, \mathbf{r}_h); \quad 53.$$

for the states with $F = -1$

$$\Psi_{-1}^{U,L}(\mathbf{r}_e, \mathbf{r}_h) = \mp i C^- \Psi_{\uparrow, -3/2}(\mathbf{r}_e, \mathbf{r}_h) + C^+ \Psi_{\downarrow, -1/2}(\mathbf{r}_e, \mathbf{r}_h), \quad 54.$$

where

$$C^\pm = \sqrt{\frac{\sqrt{f^2 + d} \pm f}{2\sqrt{f^2 + d}}}, \quad 55.$$

$f = (-2\eta + \Delta)/2$ and $d = 3\eta^2$. The energies and size dependence of the two $F = 0$ exciton levels are given by:

$$\varepsilon_0^{U,L} = \eta/2 + \Delta/2 \pm 2\eta, \quad 56.$$

(we denote the two $F = 0$ states by 0^U and 0^L), with corresponding wave functions:

$$\Psi_0^{U,L}(\mathbf{r}_e, \mathbf{r}_h) = \frac{1}{\sqrt{2}} [\mp i \Psi_{\uparrow, -1/2}(\mathbf{r}_e, \mathbf{r}_h) + \Psi_{\downarrow, 1/2}(\mathbf{r}_e, \mathbf{r}_h)]. \quad 57.$$

The size dependence of the band edge exciton splitting for hexagonal CdSe crystals with different shapes is shown in Figure 13 (46). The calculation was done using $\beta = 0.28$ (22). In spherical crystals (Figure 13a) the $F = \pm 2$ state is the exciton ground state for all sizes and is optically passive (51). The separation between the ground state and the lower optically active $F = \pm 1$ state initially increases with decreasing size as $1/a^3$ but tends to $3\Delta/4$ for very small crystals.

Actually Figure 13a already resolves the experimental puzzle, which was addressed in (41). The exciton ground state has an angular momentum projection ± 2 and is optically passive. Called a Dark Exciton, it cannot be excited by a photon and cannot directly recombine radiatively because emitted and absorbed photons cannot have an angular momentum 2. Therefore we must optically excite one of the upper exciton states that then thermalizes to the optically forbidden ground dark state, which has a long radiative decay time. The Stokes shift is the splitting between the ± 2 exciton state and the lowest ± 1 optically active Bright Exciton.

In oblate crystals (Figure 13b) the order of the exciton levels is the same as in spherical ones. However, the splitting does not saturate, because in these crystals, Δ increases with decreasing size. In prolate crystals Δ becomes negative with decreasing size, and this changes the order of the exciton levels at some value of the radius (Figure 13c); in small crystals the optically passive (see below) $F = 0$ state becomes the ground exciton state. This crossing occurs when Δ goes through 0. In Figure 13d the band edge exciton fine structure is shown for the case where the ellipticity depends on the size corresponding to SAXS and TEM measurements of the CdSe crystals (56): $\mu(a) = 0.101 - 0.034a + 3.507 \cdot 10^{-3}a^2 - 1.177 \cdot 10^{-4}a^3 + 1.863 \cdot 10^{-6}a^4 - 1.418 \cdot 10^{-8}a^5 + 4.196 \cdot 10^{-11}a^6$. The level structure here closely resembles that of spherical crystals.

Figure 14 shows a comparison of the theoretical Stokes shifts (the splitting between the ± 2 exciton state and the lowest ± 1 optically active Bright Exciton) (Figure 13d) with experimental data obtained at resonant excitation within

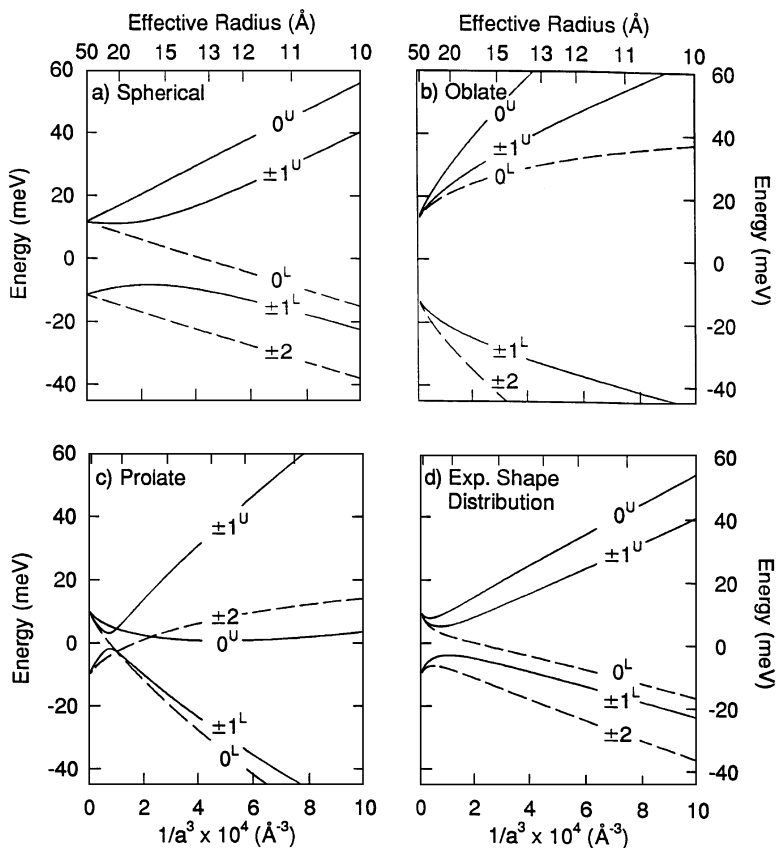


Figure 13 The size dependence of the exciton band edge structure in ellipsoidal hexagonal CdSe quantum dots with ellipticity μ : (a) spherical dots ($\mu = 0$); (b) oblate dots ($\mu = -0.28$); (c) prolate dots ($\mu = 0.28$); (d) dots having a size-dependent ellipticity determined from SAXS and TEM measurements. Solid (dashed) lines indicate optically active (passive) levels (46).

the absorption band edge tail of the CdSe nanocrystals (43). Figure 14a shows the photoexcitation spectra for several crystal sizes. There is good quantitative agreement between experiment and theory for large sizes. For the smaller crystals, however, the theoretical splitting based on the size-dependent exchange interaction underestimates the observed Stokes shift. This discrepancy may be explained, in part, by an additional contribution to the Stokes shift by acoustic phonons.

Bright and Dark Exciton States

To describe the fine structure of the absorption spectra and photoluminescence one needs to calculate the transition oscillator strengths of these five exciton states.

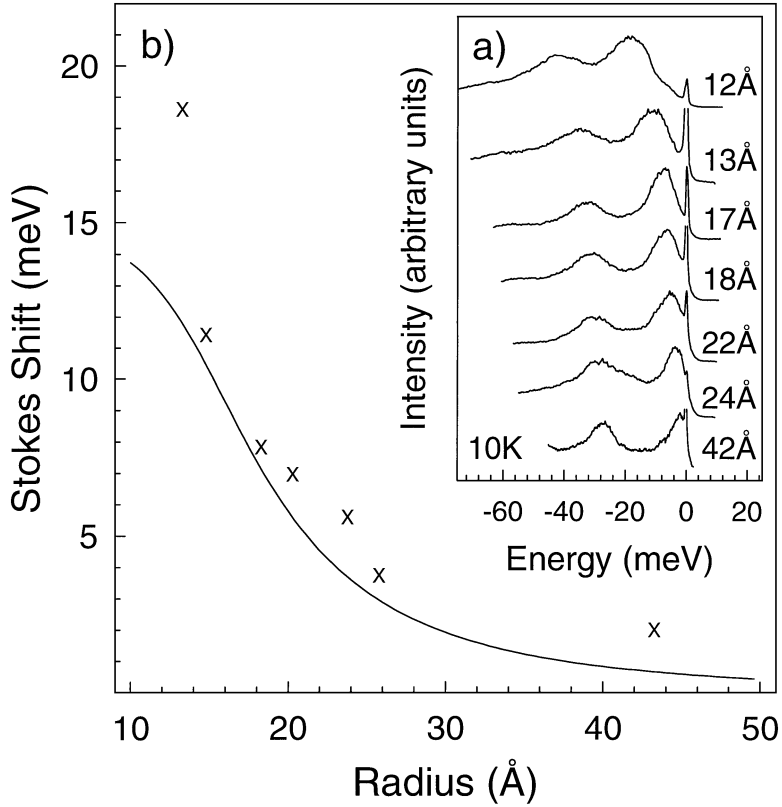


Figure 14 (a) Normalized FLN spectra for CdSe nanocrystals between 12 and 42 Å in radius. (b) The size dependence of the resonant Stokes shift. The Stokes shift is the difference in energy between the pump energy and the peak of the zero phonon line in the FLN measurements. The points labeled X are the experimental values. The solid line is the theoretical size-dependent splitting between the $\pm 1^L$ state and the ± 2 exciton ground state (see Figure 2d) (43).

The mixing of the electron and hole spin momentum states by the electron-hole exchange interaction strongly affects the optical transition probabilities. The wave functions of the $|F| = 2$ exciton state, however, are unaffected by this interaction (see Equation 51); it is optically passive in the dipole approximation because emitted and absorbed photons cannot have an angular momentum projection of ± 2 . The probability of the optical excitation or recombination of an exciton state with total angular momentum projection F is proportional to the square of the matrix element of the momentum operator $\mathbf{e}\hat{\mathbf{p}}$ between that state and the vacuum state:

$$P_F = |\langle 0 | \mathbf{e}\hat{\mathbf{p}} | \Psi_F \rangle|^2, \quad 58.$$

where $|0\rangle = \delta(\mathbf{r}_e - \mathbf{r}_h)$, \mathbf{e} is the polarization vector of the emitted or absorbed photon, the momentum operator $\hat{\mathbf{p}}$ acts only on the valence band Bloch functions (see Equation 6), and the exciton wave function, $\tilde{\Psi}_F$, is written in the electron-electron representation. Exciton wave functions in the electron-hole representation are transformed to the electron-electron representation by taking the complex conjugate of Equations 51, 53, 54, and 57 and flipping the spin projections in the hole Bloch functions (\uparrow and \downarrow to \downarrow and \uparrow).

For the exciton state with $F = 0$ we obtain (46)

$$P_0^{U,L} = |\langle 0 | \mathbf{e} \hat{\mathbf{p}} | \tilde{\Psi}_0^{U,L} \rangle|^2 = \frac{(1 \pm 1)^2}{3} K P^2 \cos^2(\theta), \quad 59.$$

where $P = m_0 V$, θ is the angle between the polarization vector of the emitted or absorbed photon and the hexagonal axis of the crystal, and K is the square of the overlap integral (51):

$$K = \frac{2}{a} \left| \int dr r \sin(\pi r/a) R_0(r) \right|^2. \quad 60.$$

The overlap integral is independent of crystal size and depends only on β . Hence, the excitation probability of the $F = 0$ state does not depend on crystal size. For the lower exciton state, 0^L , it is identically zero. At the same time the exchange interaction increases the excitation probability of the upper 0^U exciton state by a factor of four. This result arises from the constructive and destructive interference of the wave functions of the two indistinguishable exciton states $|\uparrow, -1/2\rangle$ and $|\downarrow, 1/2\rangle$ (see Equation 57).

For the exciton state with $F = 1$ we obtain (46)

$$P_1^{U,L} = \frac{1}{3} \left(\frac{2\sqrt{f^2 + d} \mp f \pm \sqrt{3d}}{2\sqrt{f^2 + d}} \right) K P^2 \sin^2(\theta). \quad 61.$$

The excitation probability of the $F = -1$ state is equal to that of the $F = 1$ state. As a result, the total transition probability for the doubly degenerate $|F| = 1$ exciton states is equal to $2P_1^{U,L}$.

Equations 59 and 61 show that the $F = 0$ and $|F| = 1$ state excitation probabilities differ in their dependence on the angle between the light polarization vector and the hexagonal axis of the crystal. If the crystal hexagonal axes are aligned perpendicular to the light direction, only the active $F = 0$ state can be excited. Alternatively, if the crystals are aligned along the light propagation direction, only the upper and lower $|F| = 1$ states will participate in the absorption. For the case of randomly oriented crystals, polarized excitation resonant with one of these exciton states selectively excites suitably oriented crystals, which leads to polarized luminescence (51). Observation of this effect has been reported in several papers (57, 44). Furthermore, the large energy splitting between the $F = 0$ and $|F| = 1$ states can lead to different Stokes shifts in the polarized luminescence.

To find the probability of exciton excitation for a system of randomly oriented nanocrystals, we must average Equations 59 and 61 over all possible solid angles. The respective excitation probabilities are proportional to (46)

$$\begin{aligned} \overline{P_0^{U,L}} &= \frac{(1 \pm 1)^2 K P^2}{9}, \\ \overline{P_1^{U,L}} &= \overline{P_{-1}^{U,L}} = \frac{2K P^2}{9} \left(\frac{2\sqrt{f^2 + d} \mp f \pm \sqrt{3d}}{2\sqrt{f^2 + d}} \right). \end{aligned} \quad 62.$$

There are three optically active states with relative oscillator strengths $\overline{P_0^U}$, $2\overline{P_1^U}$, and $2\overline{P_1^L}$. The size dependence of these strengths for different shapes is shown in Figure 15 for hexagonal CdSe crystals. Clearly the crystal shape strongly influences this dependence. For example, in prolate crystals (Figure 15c) the $\pm 1^L$ state oscillator strength goes to zero in crystals of radius such that $\Delta = 0$; i.e. where the crystal shape asymmetry exactly compensates the crystal field asymmetry of the hexagonal lattice structure. One can see that for all nanocrystal shapes the excitation probability of the lower $|F| = 1 (\pm 1^L)$ exciton state, $2\overline{P_1^L}$, decreases with size and that the upper $|F| = 1 (\pm 1^U)$ gains its oscillator strength.

Dark Exciton Lifetime in Magnetic Field

Further strong evidence of this model is found in the study of fluorescence line narrowing (FLN) and in the decay of the photoluminescence in a magnetic field (43, 46). Figure 16a shows the magnetic field dependence of the FLN for 12 Å radius CdSe nanocrystals in magnetic fields from 0–10 T. Each spectrum is normalized to the one phonon line at zero field. In isolation, the ± 2 state would have an infinite lifetime in the electric dipole approximation, because the emitted photon cannot carry off an angular momentum of 2. However, the Dark Exciton can recombine via an LO-phonon-assisted angular momentum-conserving transition (51). Spherical LO phonons with orbital angular momenta of 1 or 2 (58, 59) are expected to participate in these transitions. Consequently, for zero field the LO phonon lines are strongly enhanced relative to the zero phonon line (ZPL). However, an external magnetic field mixes the ± 2 level and optically active ± 1 states in dots whose hexagonal axes are not parallel to the magnetic field, diminishing the need of LO phonon-assisted recombination. This explains the dramatic rise of the ZPL intensity relative to the higher LO phonon replicas with increasing field.

The magnetic field-induced admixture of the optically active ± 1 states shortens the exciton radiative lifetime. Luminescence decays for 12 Å radius crystallites in an external magnetic field between 0 and 10 T at 1.7 K are shown in Figure 16b. The sample was excited far to the blue of the first absorption maximum to avoid orientational selection in the excitation process because the transition dipole of the $|F| = 1$ states is perpendicular to the hexagonal axis. Excitons rapidly thermalize to the ground state through acoustic and optical phonon emission. The long μs luminescence at zero field is consistent with LO phonon-assisted recombination from this state. Although the light emission occurs primarily from the ± 2 state,

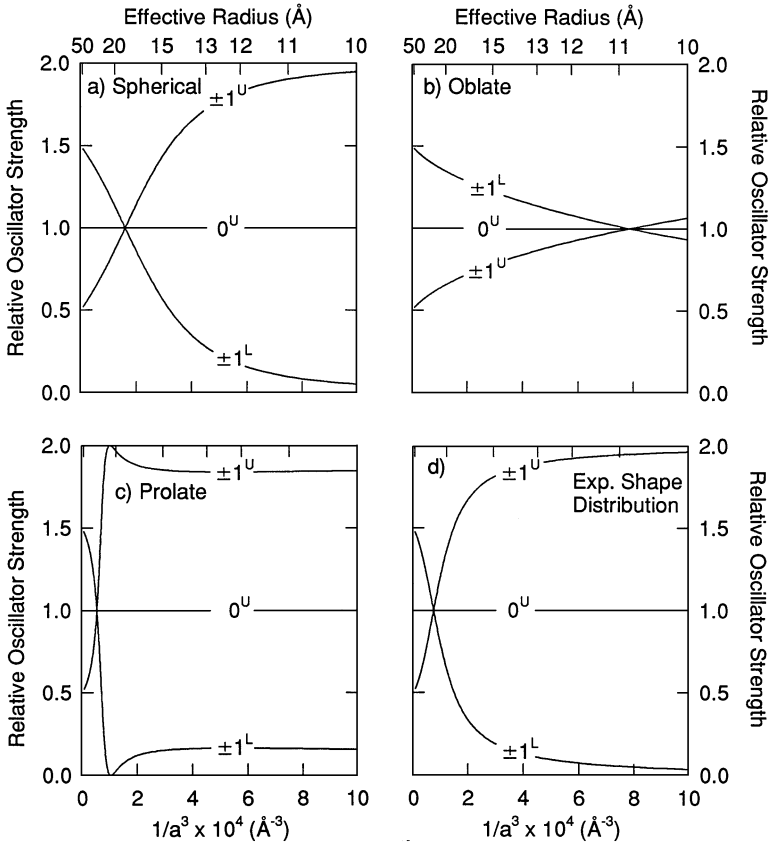


Figure 15 The size dependence of the oscillator strengths, relative to the that of the 0^U state, for the optically active states in hexagonal CdSe quantum dots with ellipticity μ : (a) spherical dots ($\mu = 0$); (b) oblate dots ($\mu = -0.28$); (c) prolate dots ($\mu = 0.28$); (d) dots having a size-dependent ellipticity determined from SAXS and TEM measurements (46).

its long radiative lifetime allows the thermally partially populated $\pm 1^L$ state also to contribute to the luminescence. With increasing magnetic field the luminescence lifetime decreases; since the quantum yield remains essentially constant, this implies that this emission is due to an enhancement of the radiative rate.

The admixture of active ± 1 Bright Exciton states into the Dark Exciton can be calculated. It is proportional to the square of magnetic field, and depends on the electron and hole g-factors and the parameters of the exciton fine structure. The admixture depends on the angle between magnetic field and the hexagonal crystal axis (43, 46), which leads to a nonexponential dependence of the luminescence decay on time. Using this admixture and 3-level kinetics (43), the PL decay at 10 T

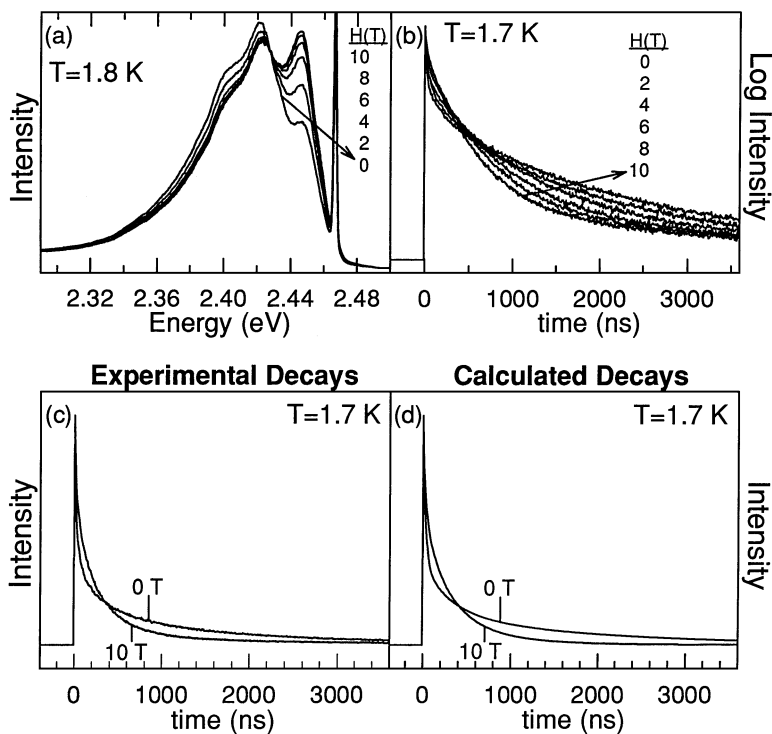


Figure 16 (a) FLN spectra for 12 Å radius CdSe nanocrystals as a function of external magnetic field. The spectra are normalized to their one phonon line (1PL). A small fraction of the excitation laser, which is included for reference, appears as the sharp feature at 2.467 eV to the blue of the zero phonon line (ZPL). (b) Luminescence decays for 12 Å radius dots (for magnetic fields between 0 and 10 T) measured at the peak of the full luminescence (2.436 eV) and for a pump energy of 2.736 eV. All experiments were done in the Faraday configuration ($\mathbf{H} \parallel \mathbf{k}$); (c) Observed luminescence decays for 12 Å radius dots at 0 and 10 T; (d) calculated decays based on a 3-level model (43).

for 12 Å radius crystals is reproduced (see Figures 16c,d). The field-dependent decay was calculated averaging over the random orientation of the crystal axes, using bulk value for the electron g-factor and the calculated exciton fine structure.

DOPED NANOCRYSTALS

Although techniques for growing different types of pure semiconductor nanocrystals are very well developed (for example see 1), the problem of how to dope them is not resolved at present. Self-purification is an intrinsic thermodynamic property of nanocrystals; any heat treatment increases the diffusion of impurities,

intrinsic structural defects and dislocations and easily pushes them to the nearby surface. This makes the doping of semiconductor quantum dots a serious technological problem. Doping has to be done at low temperatures, and all further heat treatment of the samples must be avoided. Preparation of the nanocrystals by organometallic reactions at room temperature seems to be a way to overcome this problem, and the first successful Mn doping of ZnS nanocrystals has been reported (60); recently another low-temperature technique, coprecipitation in a reverse micelle solution, has allowed the preparation of Mn-doped CdS nanocrystals (61, 62). The observation of the donor-acceptor recombination in CdS nanocrystals (63) also shows the possibility of residual doping of some nanocrystals.

In this section we will consider the effect of confinement on shallow and deep impurities in small nanocrystals, as well as the occurrence of internal giant effective magnetic fields produced by Mn dopants in nanocrystals.

Binding Energy of Shallow Donors

The binding energy of an electron to a shallow donor and the shape of its wave function depend strongly on the ratio of the electron Bohr radius, $a_B = \hbar^2 \kappa / m_e e^2$ to the crystal radius (63). In the weak confinement regime, $a_B \ll a$, the binding energy is described almost everywhere in crystal by the hydrogen-like expression $E_B = e^4 m_e / 2 \kappa^2 \hbar^2$. Only in the narrow shell, of width $\sim a_B$, near the crystal surface does the binding energy decrease rapidly; at the surface the donor energy is given (63)

$$E_b = -\frac{E_B}{4} + \frac{3}{64} \frac{a_B}{a} E_B. \quad 63.$$

In the opposite limit of strong confinement, when $a \ll a_B$, the energy of the electron size quantization, $\hbar^2 \pi^2 / 2 m_e a^2$ is much greater than the energy of its interaction with an impurity $\sim e^2 / \kappa a$. In this case the electron is delocalized and its wave function goes over the whole crystal volume. The electron motion is described by the wave function, $\xi(\mathbf{r})$ (see Equation 36), of the lowest electron QSL. The energy of the electron interaction with the donor can be found to first order in perturbation theory:

$$\delta E = -\frac{e^2}{\kappa} \int d^3 r \frac{\xi^2(\mathbf{r})}{|\mathbf{r} - \mathbf{d}|} = -\frac{e^2}{\kappa a} f(d/a), \quad 64.$$

where \mathbf{d} is the donor position and $f(x) = 1 - \sin(2\pi x)/(2\pi x) + \text{Cin}(2\pi) - \text{Cin}(2\pi x)$, where $\text{Cin}(x)$ is a cosine integral and varies from $f(0) \approx 2.4$ to $f(1) = 1$. As a result, for $a \ll a_B$, the donor ground state energy can be written (63)

$$E_b(d) = \frac{\hbar^2 \pi^2}{2 m_e a^2} - \frac{e^2}{\kappa a} f\left(\frac{d}{a}\right). \quad 65.$$

It is important to note that numerical calculations (63) show that Equation 65 works very well also in intermediate size crystals and describes the donor binding energy in crystals with radius smaller than $a < 3a_B$.

Deep Centers and PL decay in Nanocrystals

If the radius of the deep acceptor or defect, a_h , is much smaller than the crystal radius, then its wave function and binding energy is almost unaffected by confinement. However, the confinement may strongly effect the absorption cross section of such localized defects. This is connected with the increase of the free electron or hole wave function overlap with the defect wave function with decreasing radius; the overlap is inversely proportional to the nanocrystal volume.

One of these effects has been seen experimentally—the shortening with decreasing size of the free electron-acceptor recombination time in CdS nanocrystals (63). For two different acceptors it was shown that the free electron-acceptor radiative decay can be described by the characteristic time $\tau \sim (a/a_h)^3$, where $a_h = \sqrt{\hbar^2/2m_{hh}E_A}$ is the radius of the deep acceptor with binding energy E_A .

Giant Spin Sublevel Splitting in Mn-Doped Nanocrystals

A great enhancement of short-range spin-spin contact interactions is one of the most interesting properties of low-dimensional semiconductor structures. Confinement of the electron and hole wave functions enhances this interaction such that it is inversely proportional to the volume of the nanocrystal. For example, the enhancement of the electron-hole exchange interaction in nanocrystals leads to formation of the optically forbidden Dark Exciton, which was discussed above. Even stronger effects are seen as a result of the enhancement of the short-range spin-spin interaction of confined electrons and holes with a magnetic ion. The effective magnetic field of a single magnetic ion acting on the electron can be written:

$$\mathbf{H} = (\mu_B g_e)^{-1} v_0 \alpha_{exch}^{ion} \mathbf{S} \xi_e^2(\mathbf{r}), \quad 66.$$

where $\xi_e(\mathbf{r})$ is the electron wave function at the ion position, \mathbf{S} is the spin of magnetic ion, α_{exch}^{ion} is on the order of several eV, μ_B is the Bohr magneton, and g_e is the electron g -factor. One can see that the effective magnetic field is parallel to the ion spin direction, that its magnitude depends on the ion position in the nanocrystal, and that it grows as $1/a^3$. Calculations show that the field inside a nanocrystal containing a single dopant ion can reach thousands of tesla and splits the electron spin sublevels by as much as 10–100 meV.

The effective magnetic field acting on a hole cannot generally be written in such a simple form because of the strong spin-orbit interaction in the valence band. The effective magnetic field acting on a hole is not parallel to the spin direction of the magnetic ion and has a complicated dependence on the ion position in the nanocrystal (AL Efros & M Rosen, unpublished data). Nevertheless it also grows as $1/a^3$, reaches thousands of tesla and splits hole sublevels by as much as 100 meV.

This splitting of the electron and hole spin sublevels exists in zero external magnetic fields. How is it observed? Because of the random orientation of the magnetic ion spins in an ensemble of nanocrystals, unpolarized and even circularly

polarized light will excite transitions between all possible spin sublevels. As a result, only a broadening of the absorption spectrum of the allowed transitions instead of a splitting is seen in zero magnetic field.

To observe a splitting, we need to establish a well defined spatial direction recognized by the system. We do this by applying an external magnetic field, B , which aligns all the ion spins along the direction of the field. Selection rules can then be written, and circularly polarized light will excite the appropriate individual components of the spin sublevels in accordance with the appropriate selection rules. A comparison of the absorption of right and left circularly polarized light exhibits the spin sublevel splitting. The degree of the spin alignment of the magnetic ions is governed by the Brillouin function, $B_S(x)$:

$$\langle S \rangle = SB_S \left(\frac{g\mu_B SB}{kT} \right), \quad 67.$$

which depends on the ratio of the magnetic energy, $g\mu_B SB$ to the temperature, T , where g is the magnetic ion g -factor. The Brillouin function $B_S(x) = 1$ when $x \gg 1$, so that at low temperature or high magnetic field one can reach 100% alignment (if the nanocrystals contain a single magnetic ion). This allows us to measure the value of the sublevel splitting.

Maximum splitting occurs when the ion is at the center of the nanocrystal. Existing technology does not allow us to make such crystals at present; we must assume that the ions can occupy any possible metal site in the crystal. Assuming equal probability for all ion positions, we obtain an observed splitting of the electron and hole spin sublevels, which is six times smaller than the maximum value:

$$\Delta E_{e,h} = \alpha_{exch}^{ion}(e, h) S \frac{3v_0}{16\pi a^3}. \quad 68.$$

This is assuming that the nanocrystals contain only a single magnetic ion. Isolation of the ions in a nanocrystal is important. Increasing the magnetic ion concentration in bulk leads to pairing and to a decrease in the effective magnetic field.

It is not easy to avoid this effect. Statistically, even if we have one magnetic ion per crystal on the average, some nanocrystals will contain no magnetic ions at all, and some will have two or more ions. Even at a concentration that gives one ion per nanocrystal, on the average, 38% will be empty, 38% will have one ion, and 20% will have two magnetic ions. This last group of crystals decreases the observed average effective magnetic field for the ensemble.

In conclusion, the presence of a magnetic ion dopant results in a giant effective magnetic field, which splits the electron and hole sublevels by as much as 100 meV in small nanocrystals. This field leads to a giant Faraday effect and magneto circular dichroism, which have been observed in the Mn-doped CdS nanocrystals (64). To maximize this field, one should have a single magnetic ion per crystal sitting at the crystal center.

CONCLUDING REMARKS

The purpose of this review is to describe our understanding of the electronic level structure in nanosize semiconductor nanocrystals. We have not discussed the spectra of acoustical and optical phonons and their interaction with electron-hole pairs, or the role played by Auger processes in the kinetics of thermalization and interband relaxation of carriers. These processes strongly effect the photoluminescence properties of nanocrystals.

Although many aspects of the electronic structure of semiconductor nanocrystals have been fairly well described theoretically, we would like to list "clouds" that spoil this picture. First, there is no proper theoretical description of the optical properties of Si and Ge nanocrystals (or, generally speaking of nanocrystals of indirect semiconductors). Nor is there a good understanding of the boundary conditions that would let us account reliably for the leakage of the electron and hole wave functions out of the nanocrystals. Second, there is no self-consistent theory of the electron-hole Coulomb interaction in nanocrystals, which should allow us to describe the absolute value of interband transition energies, nor is there a self-consistent theory of long-range electron-hole exchange interaction that may affect the fine structure of the band edge exciton. The theoretical solution of these problems is of great importance for semiconductor nanocrystals.

ACKNOWLEDGMENTS

We would like to thank our long-term collaborators: AI Ekimov, MG Bawendi, D Norris, M Nirmal, P Alivisatos, U Banin, G Bryant, and P Sercel, as well as L Brus, whose challenging discussions stimulated most of these theoretical studies. We also thank AI Ekimov and D Norris for helping us with the figures.

Visit the Annual Reviews home page at www.AnnualReviews.org

LITERATURE CITED

1. Brus LE. 1991. *Appl. Phys. A* 53:465–74
2. Alivisatos AP. 1996. *Science* 271:933–37
3. Ekimov AI, Onushchenko AA, Tzheomskii AV. 1980. *Sov. Phys. Chem. Glass* 6:511–12
4. Henglein A. 1982. *Ber. Bunsenges. Phys. Chem.* 88:301–5
5. Itoh T, Kirihara T. 1984. *J. Lumin.* 31/32: 120–22
6. Efros AIL, Efros AL. 1982. *Sov. Phys. Semicond.* 16:772–78
7. Brus LE. 1983. *J. Chem. Phys.* 79: 5566–71
- 7a. Murray CB, Norms DG, Bawendi MG 1993. *J. Am. Chem. Soc.* 115:8706–15
8. Ekimov AI, Efros AIL, Onushchenko AA. 1985a. *Solid State. Commun.* 56: 921–24
9. Ekimov AI, Onushchenko AA. 1981. *JETP Lett* 34:345–49
10. Ekimov AI, Onushchenko AA. 1982. *Sov. Phys. Semicond.* 16:775–78

11. Ekimov AI, Onushchenko AA, Plukhin AG, Efros AIL. 1985. *Sov. Phys. JETP* 61:891–97
12. Itoh T, Iwabuchi Y, Kirihaara T. 1988. *Phys. Status Solidi B* 146:531–43
13. Ekimov AI, Onushchenko AA, Efros AIL. 1986. *JETP Lett.* 43:376–79
14. Ekimov AI, Onushchenko AA, Shumilov SK, Efros AIL. 1987. *Sov. Tech. Phys. Lett.* 13:115–16
15. Ekimov AI, Efros AIL, Ivanov MG, Onushchenko AA, Shumilov SK. 1989. *Solid State Commun.* 69:565–68
16. Ekimov AI, Onushchenko AA. 1984. *JETP Lett.* 40:1136–40
17. Luttinger JM, Kohn W. 1955. *Phys. Rev.* 97:869–83
18. Xia JB. 1989. *Phys. Rev. B* 40:8500–7
19. Grigoryan GB, Kazaryan E, Efros AIL, Yazeva TV. 1990. *Sov. Phys. Solid State* 32:1031–35
20. Ekimov AI, Hache F, Schanne-Klein MC, Ricard D, Flytzanis C, et al. 1993. *J. Opt. Soc. Am. B* 10:100–7
21. Norris DJ, Sacra A, Murray CB, Bawendi MG. 1994. *Phys. Rev. Lett.* 72:2612–15
22. Norris DJ, Bawendi MG. 1996. *Phys. Rev. B* 53:16338–46
23. Ekimov AI. 1991. *Phys. Scr.* 39:217–22
24. Rodrigues PAM, Tamulaitis G, Yu PY, Risbud SH. 1995. *Solid State Commun.* 94:583–87
25. Pidgeon CR, Brown RN. 1966. *Phys. Rev.* 146:575–83
26. Aggarwal RL. 1974. Semiconductor and semimetals. In *Modulation Techniques*, ed. PK Willardson, AC Beer, 9:151–255. New York: Academic
27. Sercel PC, Vahala KJ. 1990. *Phys. Rev. B* 42:3690–710
28. Vahala KJ, Sercel PC. 1990. *Phys. Rev. Lett.* 65:239–43
29. Kang I, Wise FW. 1997. *J. Opt. Soc. Am.* 14:1632–46
30. Efros AIL, Rosen M. 1998. *Phys. Rev. B* 58:7120–35
31. Banin U, Lee JC, Guzelian AA, Kadavani AV, Alivisatos AP, et al. 1998. *J. Chem. Phys.* 109:2036–40
32. Kane EO. 1957. *J. Phys. Chem. Solids* 1:249–61
33. Bir GL, Pikus GE. 1975. *Symmetry and Strain-Induced Effects in Semiconductors*. New York: Wiley
34. Sheka VI, Sheka DI. 1967. *Sov. Phys. JETP* 24:975–81
35. Edmonds AR. 1957. *Angular Momentum in Quantum Mechanics*. Princeton, NJ: Princeton Univ. Press
36. Kokhanovskii, Makushenko YM, Seisyan RP, Efros AIL, Yazeva TV, Abdulaev MA. 1991. *Sov. Phys. Solid State* 33:967–75
37. Richard T, Lefebvre P, Mathieu H, Allegre J. 1996. *Phys. Rev. B* 53:7287–98
38. Sercel PC, Efros AIL, Rosen M. 1999. *Phys. Rev. Lett.* 83:2394–98
39. Landolt-Börstein. 1982. *Numerical Data and Functional Relationships in Science and Technology*, ed. O Madelung. Berlin: Springer-Verlag
40. Schmitt-Rink S, Miller DAB, Chemla DS. 1987. *Phys. Rev. B* 35:8113–25
41. Bawendi MG, Wilson W, Rothberg L, Carroll DJ, Jedju TM, et al. 1990. *Phys. Rev. Lett.* 65:1623–26
42. Hasselbarth A, Eychmüller A, Weller H. 1993. *Chem. Phys. Lett.* 203:271–76
43. Nirmal M, Norris DJ, Kuno M, Bawendi MG, Efros AIL, Rosen M. 1995. *Phys. Rev. Lett.* 75:3728–31
44. Chamarro M, Gourdon C, Lavallard P, Ekimov AI. 1995. *Jpn. J. Appl. Phys.* 34:285–86
45. Chamarro M, Gourdon C, Lavallard P, Lubinskaya O, Ekimov AI. 1996. *Phys. Rev. B* 53:1336–42
46. Efros AIL, Rosen M, Kuno M, Nirmal M, Norris DJ, Bawendi MG. 1996. *Phys. Rev. B* 54:4843–56
47. Micic OI, Cheong HM, Fu H, Zunger A, Sprague JR, Mascarenhas A, Nozik AJ. 1997. *J. Phys. Chem. B* 101:4904–12
48. Banin U, Lee JC, Guzelian AA, Kadavani AV, Alivisatos AP. 1997.

- Superlattices and Microstructures* 22: 559–67
49. Calcott PDJ, Nash KJ, Canham LT, Kane MJ, Brumhead D. 1993. *J. Phys. Condens. Matter* 5:L91–93
50. Kovalev D, Heckler H, Ben-Chorin M, Polisski G, Schwartzkopff M, Koch F. 1998. *Phys. Rev. Lett.* 81:2803–6
51. Efros AIL. 1992. *Phys. Rev. B* 46:7448–58
52. Efros AIL, Rodina AV. 1989. *Solid State Commun.* 72:645–49
53. Efros AIL, Rodina AV. 1993. *Phys. Rev. B* 47:10005–7
54. Rashba EI. 1959. *Sov. Phys. JETP* 9:1213–16
55. Kochereshko VP, Mikhailov GV, Ural'tsev IN. 1983. *Sov. Phys. Solid State* 25:439–42
56. Murray CB, Norris DJ, Bawendi MG. 1993. *J. Am. Chem. Soc.* 115:8706–15
57. Bawendi MG, Carroll PJ, Wilson WL, Brus LE. 1992. *J. Chem. Phys.* 96:946–54
58. Klein MC, Hache F, Ricard D, Flytzanis C. 1990. *Phys. Rev. B* 42:11123–32
59. Efros AIL. 1993. In *Phonons in Semiconductor Nanostructures*, ed. JP Leburton, J Pascual, C Sotomayor-Torres, pp. 299–308. Boston/London: Kluwer
60. Bhargava RN, Gallagher D, Hong X, Nurmikko A. 1994. *Phys. Rev. Lett.* 72:416–419
61. Counio G, Esnouf S, Gacoin T, Boilot JP. 1996. *J. Chem. Phys.* 100:20021–26
62. Counio G, Gacoin T, Boilot JP. 1998. *J. Chem. Phys.* 102:5257–60
63. Ekimov AI, Kudryavtsev IA, Ivanov MG, Efros AIL. 1990. *J. Lumin.* 46:83–95
64. Hoffman DM, Meyer BK, Ekimov AI, Merkulev IA, Efros AIL, et al. 2000. *Solid State Commun.* Submitted



CONTENTS

The Theory of Real Materials, <i>Marvin L. Cohen</i>	1
Tribochemical Polishing, <i>Viktor A. Muratov, Traugott E. Fischer</i>	27
High-Tc Superconductivity in Electron-Doped Layered Nitrides, <i>Shoji Yamanaka</i>	53
Holographic Polymer-Dispersed Liquid Crystals (H-PDLCs), <i>T. J. Bunning, L. V. Natarajan, V. P. Tondiglia, R. L. Sutherland</i>	83
Optical Generation and Characterization of Acoustic Waves in Thin Films: Fundamentals and Applications, <i>John A. Rogers, Alex A. Maznev, Matthew J. Banet, Keith A. Nelson</i>	117
Structure Evolution During Processing of Polycrystalline Films, <i>C. V. Thompson</i>	159
Mechanical Behavior of Metallic Foams, <i>L. J. Gibson</i>	191
Copper Metallization for High-Performance Silicon Technology, <i>R. Rosenberg, D. C. Edelstein, C.-K. Hu, K. P. Rodbell</i>	229
The Properties of Ferroelectric Films at Small Dimensions, <i>T. M. Shaw, S. Trolier-McKinstry, P. C. McIntyre</i>	263
IC-Compatible Polysilicon Surface Micromachining, <i>J. J. Sniegowski, M. P. de Boer</i>	299
SiGe Technology: Heteroepitaxy and High-Speed Microelectronics, <i>P. M. Mooney, J. O. Chu</i>	335
Ultrathin Diffusion Barriers/Liners for Gigascale Copper Metallization, <i>A. E. Kaloyeros, E. Eisenbraun</i>	363
Magnetocaloric Materials, <i>K. A. Gschneidner Jr., V. K. Pecharsky</i>	387
Advances in In Situ Ultra-High Vacuum Electron Microscopy: Growth of SiGe on Si, <i>Ruud M. Tromp, Frances M. Ross</i>	431
Layered Magnetic Manganites, <i>T. Kimura, Y. Tokura</i>	451
The Electronic Structure of Semiconductor Nanocrystals, <i>Al. L. Efros, M. Rosen</i>	475
Mechanisms for Enhanced Formation of the C45 Phase of Titanium Silicide Ultra-Large-Scale Integration Contacts, <i>J. M. E. Harper, C. Cabral Jr., C. Lavoie</i>	523
Synthesis and Characterization of Monodisperse Nanocrystals and Close-Packed Nanocrystal Assemblies, <i>C. B. Murray, C. R. Kagan, M. G. Bawendi</i>	545
Extremely High Density Longitudinal Magnetic Recording Media, <i>Dieter Weller, Mary F. Doerner</i>	611
Low Dielectric Constant Materials for ULSI Interconnects, <i>Michael Morgen, E. Todd Ryan, Jie-Hua Zhao, Chuan Hu, Taiheui Cho, Paul S. Ho</i>	645
Device Innovation and Material Challenges at the Limits of CMOS Technology, <i>P. M. Solomon</i>	681